Draft version November 14, 2025
Typeset using LaTeX **default** style in AASTeX7.0.1

JWST View of the Supernebula in NGC 5253. I. Overview and Continuum Features

Jean L. Turner [1], Sara C. Beck [2], Elm Zweig [1], L. Barcos-Muñoz [3,4], John H. Black [5], Daniel P. Cohen [1], S. Michelle Consiglio [1], Nicholas G. Ferraro [1], Paul T. P. Ho [6] and David S. Meier [7]

[1] UCLA Department of Physics and Astronomy
[2] Tel Aviv University, Tel Aviv, Israel
[3] National Radio Astronomy Observatory, 520 Edgemont Road, Charlottesville, VA 22903, USA
[4] Department of Astronomy, University of Virginia, 530 McCormick Road, Charlottesville, VA 22903, USA
[5] Chalmers Institute of Technology
[6] Academia Sinica Astronomy and Astrophysics
[7] New Mexico Institute of Mining and Technology

ABSTRACT

We present imaging spectroscopy of the "supernebula" in the nearby dwarf galaxy NGC 5253 with the MIRI-MRS integral field spectrometer of the JWST. NGC 5253 is host to an luminous ($L \sim 10^9$ L$_\odot$) H II region, powered by a giant young star cluster, a possible local analogue to super star cluster formation at Cosmic Dawn and Noon. In this paper, the first in a series about the mid-infrared line and continuum emission in the center of NGC 5253, we present an overview and continuum spectra. The mid-infrared images reveal four sources of continuum emission from hot dust that we identify as luminous H II regions, which are used to define spectral apertures. The dominant continuum source is the pc-scale supernebula core seen at radio wavelengths. We find that the MIR to radio continuum flux ratio for all regions is identical to that of Galactic H II regions. The 9.7 silicate feature is present and strongest in absorption toward the supernebula. Silicate emission is seen in another H II region. PAH features are present, although weak, particularly in the supernebula; the strongest emission is in an H II region only 15 pc away. PAH features at 6.2μm and 11.3μm are detected in all sources. Comparison of the luminosity implied by the ionization to the observed infrared luminosity suggest that at least 25% of the photons are escaping the embedded supernebula core, in spite of its high, $A_V \gtrsim 15$, extinction.

1. INTRODUCTION

Giant star clusters may have been the dominant mode of star formation in the early universe, responsible for rapid heavy element enrichment and dusty galaxies at early times. Massive enough to contain thousands of O stars, these clusters are critical sources of radiation, luminosity, and feedback activity that serve to shape the host galaxy. Despite containing large numbers of active high-mass stars, these clusters not only lived to great ages to become globular clusters, but also continued to form multiple generations of stars (Bastian & Lardo 2018). What determines the limit to the size of a star cluster? How do they continue to form stars in the presence of winds and supernovae? Clusters as massive as $\sim 10^6$ M$_\odot$ are not currently forming within the Local Group; Arches Cluster and even 30 Doradus are more than an order of magnitude smaller. To find potential protoglobular clusters in formation requires extragalactic observations. The James Webb Space Telescope (JWST), with subarcsecond capability in the mid-IR, is ideal for observing the formation of these rare regions.

An excellent candidate for the study of the formation of a giant cluster in a low metallicity environment is the H II region in the nearby (3.7 Mpc) dwarf galaxy, NGC 5253. By kinematics and overall morphology, NGC 5253 is classified as a dwarf spheroidal (Caldwell & Phillips 1989). It has metallicity $Z \sim 0.3$ Z$_\odot$, similar to the Magellanic

Corresponding author: Jean Turner
turner@astro.ucla.edu

Email: turner@astro.ucla.edu

clouds (Walsh & Roy 1989; Kobulnicky et al. 1997; Monreal-Ibero et al. 2010). The similarity of the giant nebula in NGC 5253 to 30 Doradus was noted in the first spectrum ever obtained of the source (Pickering 1895). The galaxy contains dozens of massive star clusters (Caldwell & Phillips 1989; Gorjian 1996; Calzetti et al. 1997; Harris et al. 2004; Cresci et al. 2005; de Grijs et al. 2013; Calzetti et al. 2015; Smith et al. 2016), the brightest of which are blue and young, with ages of 1-30 Myrs (Calzetti et al. 1997; Harris et al. 2004; de Grijs et al. 2013). Extremely bright [S IV] emission (Aitken et al. 1982; Moorwood & Glass 1982; Beck et al. 1996) indicates that a giant cluster containing very massive stars must be present (Aitken et al. 1982; Moorwood & Glass 1982; Beck et al. 1996; Crowther et al. 1999). Nitrogen enhancement near the [S IV] source and Wolf-Rayet spectral features (Walsh & Roy 1989; Kobulnicky et al. 1997; Schaerer et al. 1997; Monreal-Ibero et al. 2010) indicates the influence of Wolf-Rayet stars. The proposal that an interaction with nearby M83 initiated the recent burst of star formation seems unlikely, given that the two galaxies are not particularly close along the line of sight and NGC 5253 is relatively "isolated" (Karachentsev et al. 2007, 2013).

High resolution imaging with the Very Large Array (VLA) (Beck et al. 1996) revealed a compact ($\sim$ 1-3 pc) radio source, the "supernebula", corresponding to an H II region far more luminous than indicated by H α emission (Calzetti et al. 1997). The radio and infrared data suggest a Lyman continuum rate for the pc-scale supernebula core consistent with a cluster of $\gtrsim$1000 O stars and $L \sim 10^9$ $L_\odot$, (Beck et al. 1996; Turner et al. 1998; Rodríguez-Rico et al. 2007). The discrepancies between Hα and IR and radio fluxes indicate a high visual extinction (Calzetti et al. 1997). The estimated extinction of $A_V \gtrsim 15$ mag is based on KECK/NIRSPEC slit spectroscopy of Brackett α and γ fluxes (Turner et al. 2003, see also Martin-Hernandez 2004 and Alonso-Herrero 2004).

Despite its population of young stars and extensive recent star formation (Harris et al. 2004), NGC 5253 is unusual in that there is very little molecular gas within the galaxy proper (Turner et al. 1997; Meier et al. 2002). The discrepancy cannot be explained by CO-dark gas, since studies of dust and H I do not indicate an unusually high conversion factor (Hunt et al. 2005). CO imaging suggests that the star formation is being fueled by stream accretion from a redshifted streamer outside the galaxy along the prominent dust lane (Turner et al. 1997; Meier et al. 2002; Turner et al. 2015, 2017; Consiglio et al. 2017; Miura et al. 2018). NGC 5253 is surrounded by a halo of filamentary neutral hydrogen (Kobulnicky & Skillman 1995, 2008; López-Sánchez et al. 2012). The "ionization cone" first noted by Graham (1981) appears to be on the surface of this infalling streamer; its excitation probably arises from the central starburst (Zastrow et al. 2011), and it is more likely an "ionization sheath" around the molecular gas. Star formation fed by stream accretion may be distinct from star formation fueled by turbulent but relatively quiescent molecular clouds in spirals. The current cluster formation in NGC 5253 appears to have a star formation efficiency of $>>$ 50-70% (Turner et al. 2017), factors of a few more efficient than Galactic star-forming regions. Stream-fed star formation may have been more dominant in the early universe.

Based on previous mid-infrared spectra revealing high excitation nebular lines (Verma et al. 2003; Martín-Hernández et al. 2005; Beirão et al. 2006), there is speculation that very massive stars (VMS) could be present in the giant H II region in NGC 5253, with masses perhaps as high as 300 $M_\odot$ (Crowther et al. 1999; Smith et al. 2016). It is also possible that, in such a massive cluster, self-enrichment could occur so quickly that catastrophic cooling could stall stellar winds and perhaps even supernova remnant expansion (Silich et al. 2004; Tenorio-Tagle et al. 2005), which could limit feedback. The evolution of the giant H II region in NGC 5253 is, for these reasons, a target of special interest. The need for a subarcsecond resolution mid-infrared (MIR) picture of this region using JWST is clear.

This paper is the first of a series describing imaging spectroscopy of the giant star cluster and nebula in NGC 5253 with the Medium Resolution Spectrometer of the Mid-Infrared Instrument (MIRI) (Wells et al. 2015; Argyriou et al. 2023a). These observations give a glimpse into the innermost workings of a giant star cluster and its environment while it is in the process of active formation. In Paper I, we provide an overview of the observations and data reduction, and the regions that will later be used as apertures for line flux determinations. We discuss the continuum emission of the region including broad solid state features and compute mid-infrared luminosities for the regions. In subsequent papers we will present the nebular and molecular emission line fluxes measured for the regions defined here, images of the line emission, and modeling of the emission from the H II regions.

2. OBSERVATIONS AND DATA REDUCTION

The Cycle 1 program JWST GO-2402 was executed in 2022 March. It consists of a single science pointing of the MIRI/MRS spectrometer and a dedicated background observation. The design and flight performance of MIRI/MRS are described in Wells et al. (2015) and Argyriou et al. (2023a). Data were taken in each of the four channels and at each of the three grating settings (short, medium, and long) for a total of twelve bands spanning the wavelength

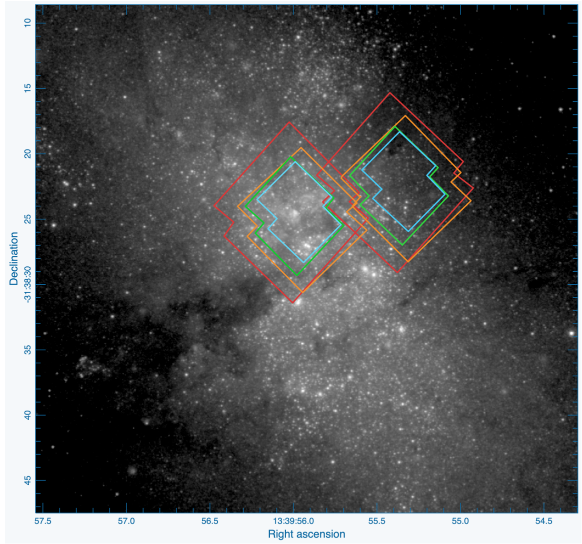

Figure 1. Footprints for the JWST MIRI/MRS cubes for the science (left) and background (right) observations. The science footprint is centered on the bright radio "supernebula" near the brightest visual source. Footprints are shown for the four channels: Bands 1-S (4.95μm; blue), 2-L (near [SIV]10.51μm; green), 3-L (near [Ne III]15.55μm; orange) and 4-L (26.0μm; red). The southeastern corner of the background has continuum and weak line emission beyond 12μm in Channels 3 and 4.

range 4.9-28μm. Observations were executed using a 4-point dither and FASTR1 readout mode, with 4 integrations of 16 seconds and a total exposure time of 477 seconds. The dedicated background was observed for an equal amount of time. The spatial resolution of MIRI/MRS ranges from 0.3$''$ at 5μm to 0.8$''$ at 27μm, full width half maximum (FWHM); spectral resolution ranges from 1300-3700, with some variation within bands (Argyriou et al. 2023a).

The science pointing was centered on the radio core in NGC 5253, which is located at R.A. $13^h39^m55\overset{s}{.}965$, Dec. -$31°38'24\overset{''}{.}364$ (ICRS). In Figure 1 we show the detector footprints of the four channels for both the science observations and the background on an HST/ACS F555W image of NGC 5253. The footprints shown span the four channels, from Band 1-S at 4.9μm, to the longest wavelength, to Band 4L at 26μm. Science and background footprints overlap in Channel 4. The background has continuum and weak line emission in the southwest corner of the footprint that affects the longer wavelengths. This necessitated the construction of a custom background, described below.

NGC 5253 is uncommonly bright in the infrared, so bright that multiple reflections within the detector gave rise to strong fringing and spatial artifacts. In addition to the "petals" of the point spread function (PSF), there are artifacts such as the cruciform (Gáspár et al. 2021) that affect the entire footprint. An additional problem was that the dedicated background contains emission in part of the footprint, particularly at longer wavelengths. We designed a data reduction scheme to mitigate these factors.

Data were processed by the standard pipeline (Gordon et al. 2015) version 1.15.0. Pipeline runs were performed on the science data with the MRS_FlightNB1 Jupyter notebook, both with and without subtraction of the dedicated background. A separate pipeline run was done for the background data only. Default pipeline parameters were used for the science data, with one exception: incoming flux from the extremely bright and near point-like continuum source in NGC 5253 was occasionally interpreted by the pipeline as cosmic ray hits, resulting in spectra with lacunae, particularly evident in Channel 3. For the final pipeline run on the science data, the parameter "det1.jump.find_showers=False" was used for the science data to eliminate the cosmic ray rejection. Although differences between the background subtraction and no background subtraction reductions were indiscernible for the main science target for the "POINT" spectral extraction from the default pipeline run, in the "EXTENDED" reduction, reduced fluxes were seen in extracted spectra due to the background in Channels 3 and 4. Differences between the background-subtracted and background-unsubtracted cases for the "EXTENDED" extraction are $\lesssim$10% for $\lambda < 15\mu$m but increase to 20% at 25μm.

To improve the background subtraction, instead of using the entire dedicated background, we created a custom background using spectra from smaller regions relatively free of emission within the background footprint. Since the same integration time was devoted to background as to the science target, there was adequate sensitivity. We selected elliptical regions to the western and northern edges of the footprint of extent ~2.5 x 1$''$ (FWHM), with shifts in the different bands to accommodate the varying band footprints. A background 1D intensity spectrum was constructed from the custom region for each band using the"MEAN" statistic of CARTA (Cube Analysis and Rendering Tool for Astronomy Comrie et al. 2025); the spectrum is shown in Figure 2. The background spectrum was loess-smoothed in R with the default degree two polynomial and tricubic weighting with a span of 30%, the minimum span that did not enhance fringing artifacts. Residuals between the loess fit and the spectrum are less than 0.6% and are dominated by weak lines. Following the "master background" method of the pipeline, the smoothed 1D custom background spectrum was broadcast over the 2D spatial footprint of the science data to form a background cube, uniform across the spatial dimensions, varying only along the spectral axis. Intensities were significantly reduced in the custom background by up to 75% over the default master background, to mid-band levels of 25 MJy/sr $\lambda < 13\mu$m, $\sim$ 50-70 MJy/sr 13-16μm, $\sim$100-200 MJy/sr for $\lambda \sim$ 17-21μm and $\sim$400-600 MJy/sr for $\lambda \sim$ 22-25μm, where the response degrades significantly. The background is slightly lower in Band 1L, 5-10 MJy/sr at 7-8μm. These intensities correspond to roughly 10% of the continuum for fainter sources D2 and D6 in these bands, and $\lesssim$ 2% of the D1 continuum in Channels 3 and 4. In terms of flux, $\lambda < 20\mu$m, the background contributes $\lesssim$0.05-0.1 Jy in Channels 1 and 2, and $\lesssim$0.4-0.6 Jy in Channels 3 and 4, respectively, over the entire 41.6 square arcsecond detector footprint "Chip" region. The background contributes 20 times less than these values in the smaller individual 0$''$.8 spectral extraction regions. The background spectra of the shorter wavelength bands in Channels 1 and 2 appear to be dominated by instrumental response, where backgrounds can be three to four times higher than mid-band values.

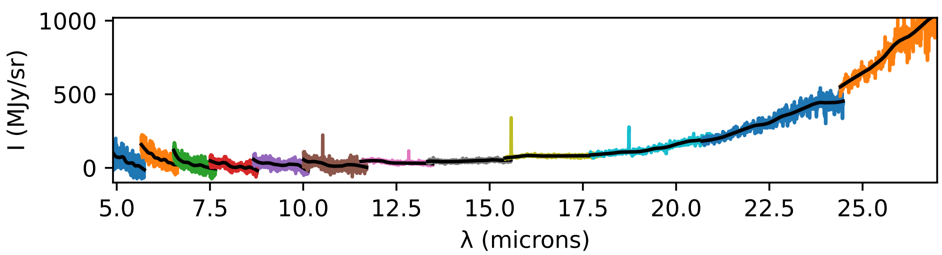

Figure 2. Custom background spectrum, computed from clean regions within the dedicated background. Mean intensity levels correspond to fluxes of $\sim$ 50mJy for $\lambda < 20\mu$m, rising to $\sim$ 0.5 Jy at 25μm, for the region corresponding to the footprint at 5μm. For the 0$''$.8 apertures used for spectral extraction, background fluxes range from 2-10 mJy from 5-28μm. Spectral lines were removed by boxcar averaging and the spectrum was loess-smoothed (black line) prior to subtraction from the science cube.

ICRS coordinates were assigned by comparison with a high resolution 1.3mm continuum image from the ALMA archive (P.I. D. Nguyen), which is largely free-free emission (Turner et al. 2017; Consiglio et al. 2017). Shifts were based on the two strongest mid-IR continuum sources using a 5.0μm continuum image constructed from the cube. The astrometry is estimated to be good to $\lesssim$ 50mas.

For each spatial region (discussed in Section 3), we obtained 1D spectra for the twelve band cubes with CARTA, using the "SUM" statistic. The 1D band spectra were corrected for fringing (Gasman et al. 2023) using the standalone package fit_residual_fringes_1d available from jwst.residual_fringe.utils. [8] The Gaussian fit procedure in Specviz was used on the individual defringed band spectra to fit line fluxes, centroids, errors, and equivalent widths. Line identifications were made by eye. The default "surroundings" baseline, generally three pixels, was assumed. Uncertainties in line fluxes were determined by repeating the Gaussian fit on a section of nearby line-free continuum of equivalent width. The lines are discussed in Paper II.

The emission is a combination of point and extended sources, so rather than use the "cone" method of flux extraction we defined fixed spatial apertures for studying spectral variations across the MIRI/MRS footprint. For MIRI/MRS it is recommended (Law et al. 2023) that an aperture larger than the observed point spread function is used to compensate for aperture broadening, undersampling, and the pull-up/pull-down effect (Argyriou et al. 2023b; Law et al. 2023; Dicken et al. 2024) in MRS cubes. These artifacts are all evident in the science data in NGC 5253. As a result, it is not possible to do pixel-by-pixel flux determinations from the cubes for these data. For the fluxes, we aimed for apertures of $\gtrsim$ 0$''$.8, the FWHM expected for the 4-S band. However, regions such as D2 and D6 near the chip edge at

[8] https://jwst-docs.stsci.edu/known-issues-with-jwst-data/miri-known-issues/miri-mrs-known-issues#gsc.tab=0

5μm were tweaked slightly to fit on the chip. Formal aperture correction factors are ∼15% for the smaller apertures (Argyriou et al. 2023a).

3. RESULTS

3.1. *The Supernebula Landscape: Gas, Dust, and Clusters*

Like a cubist painting, NGC 5253 presents different faces to observers depending on wavelength. The giant nebula has been studied extensively since its discovery (Pickering 1895; Burbidge & Burbidge 1962; Hodge 1966). The giant nebula lies in a region populated by young (∼ 10 Myr) star clusters that are bright at visible wavelengths (Caldwell & Phillips 1989; Gorjian 1996; Calzetti et al. 1999; Harris et al. 2004; de Grijs et al. 2013; Calzetti et al. 2015; Smith et al. 2016, 2020), as shown in Figure 3. Bipolar plumes of emission in H α (Calzetti et al. 1997) emerge from the center of the H II region to cover a region more than 100 parsecs in extent, criss-crossed by dust lanes. For comparison, the Great Nebula in Orion, excited by a single O star, spans about 10 pc, and 30 Doradus nebula in the LMC, a less luminous H II region, extends more than 250 pc.

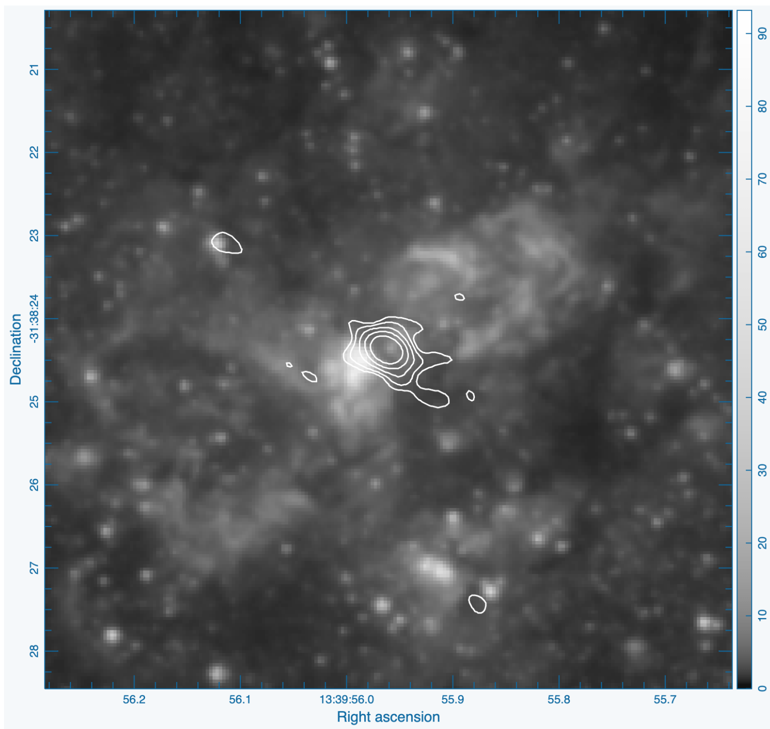

Figure 3. HST-ACS F555M image (Project 10765, P.I. Zezas) with ALMA 1.3mm continuum (Project 2017.1.00964.S, P.I. Nguyen) contours. The 1.3mm continuum is dominated by free-free emission at this resolution. Cluster 5 (Calzetti et al. 1997) is the brightest visual source, located ∼ 0.25-0.3′′ to the southeast of the radio supernebula; Cluster 11 is faint and visible near the center (Smith et al. 2020) Registration of the HST image to ICRS coordinates was done by aligning nearby Gaia stars (Cohen et al. 2018; Smith et al. 2020)

The radio view of NGC 5253 is different from the optical image. The brightest source at visible wavelengths in NGC 5253 is designated "Cluster 5" by Calzetti et al. (1997, 1999, 2015) or "Cluster 1" by Harris et al. (2004). But Cluster 5 is not the power behind the supernebula. VLA imaging reveals a bright, dense radio core, the supernebula, <1 pc in radius (Beck et al. 1996; Turner et al. 1998, 2000; Turner & Beck 2004), marking the location of a luminous and compact cluster. Contours of radio emission at $\lambda = 1.3$ mm are shown on an optical image in Figure 3. The radio core lies in a dust lane, close to, but slightly offset from, a faint optical cluster, Cluster 11 (Smith et al. 2020). The total hydrogen ionization rate implied by the radio flux is $Q_0 \sim 7 \times 10^{52}$ s^{-1}, of which ∼ 30% arises in the $r \lesssim 1$ pc radio core (Turner et al. 1998; Mohan et al. 2001; Turner & Beck 2004; Mohan et al. 2001; Rodríguez-Rico et al. 2007; Bendo et al. 2017; Turner et al. 2017). This value of Q_0 is consistent with the strong [S IV] 10.5μm emission first seen in early mid-infrared spectra (Aitken et al. 1982; Moorwood & Glass 1982; Beck et al. 1996).

The infrared continuum counterpart to the radio core was detected in subarcsecond mid-IR imaging at Keck (Gorjian et al. 2001). The brightness of the mid-IR source confirmed that the radio source was likely to be free-free emission from a compact H II region (Gorjian et al. 2001), and not, as some have proposed, an AGN. The IR core was also detected in near-infrared HST/NICMOS images (Calzetti et al. 1997; Turner & Beck 2004; Alonso-Herrero et al. 2004; Cohen et al. 2018; Smith et al. 2020). The IR core is invisible to wavelengths shorter than $\lambda \sim 1.9\mu$m (Turner & Beck 2004; Alonso-Herrero et al. 2004; Cohen et al. 2018; Smith et al. 2020). Like the radio core, the IR core is offset by $0\farcs3$ from Cluster 5 (Alonso-Herrero et al. 2004), and it is coincident with strong IR recombination line emission (Alonso-Herrero et al. 2004; Cohen et al. 2018). The cluster associated with the radio-MIR core is probably also producing the extended supernebula. Visual extinction toward the radio/IR core is estimated to be $A_V \gtrsim 15$ mag (Kawara et al. 1989; Turner et al. 2003; Alonso-Herrero et al. 2004; Martín-Hernández et al. 2005). The IR luminosity of the 100 pc region is estimated to be $\sim 10^9$ $L_\odot$ (Vanzi & Sauvage 2004; Hunt et al. 2017).

The radio-MIR core is coincident with a compact CO cloud with a radius $r < 3$ pc. This CO cloud, probably the source of the extinction toward this cluster, appears to be unusually warm and chemically peculiar (Turner et al. 2017). The CO properties suggest that the CO emission arises in photodissociation regions (PDRs) associated with molecular clumps orbiting with the stars within the H II region (Turner et al. 2015, 2017; Consiglio et al. 2017; Anderson 2016). The CO linewidth assigns a dynamical mass of 3×10^5 $M_\odot$ within the central ($r < 3$ pc cloud/H II region core (Silich et al. 2020)). This CO "cloud" could explain the high extinction to the radio core/IR cluster. However, based on extended radio emission (Meier et al. 2002) and the bipolar plumes evident in the visual, it is almost certain that this CO cloud is porous (Turner et al. 2017; Consiglio et al. 2017), allowing some photon escape.

3.2. *JWST Isolates the HII Regions within a Dusty Starburst*

High resolution HST, Keck, and ALMA observations show multiple optical, radio, and molecular line sources within the inner few arcseconds. One of our goals in this project was to isolate the embedded cluster at the core of the supernebula and observe its effects on its surroundings at cluster (5 pc) spatial scales. Mid-infrared continuum imaging is crucial for observing and characterizing the surroundings of the embedded cluster in this dusty region.

Beirão et al. (2006) presented a MIR spectrum from Spitzer of the central region of NGC 5253. The Spitzer-IRS spectra indicated high line excitation, increasing toward the central starburst region (Wu et al. 2006). However, the spatial resolution of Spitzer was unable to resolve individual pc-scale clusters, and the MIR continuum images were strongly affected by the central continuum source. Aside from the trend in increasing excitation over 30-300 pc, the slit was too wide to attribute spectral features specifically to the supernebula, although the spatial trend suggested it was the source of the high excitation.

JWST MIRI/MRS has the spatial resolution to resolve these structures at the subarcsecond level. Because MIRI/MRS is a spectrometer, MIR continuum images can be constructed for a source that would otherwise be far too bright for JWST.

MIR continuum images for each of the four channels are presented in Figure 4 at wavelengths ranging from 5μm to 20μm. The continuum images of NGC 5253 were constructed from median averages of line-free regions (at $R=\lambda/\Delta\lambda \sim 100$) from the MIRI/MRS cubes. Even at spectroscopic resolution, JWST is so sensitive that the brightness of the supernebula source affects data across the MIRI/MRS footprint and imaging artifacts are evident: the "petals" of the PSF around the central supernebula and the cruciform artifact due to reflections within the detector (Gáspár et al. 2021) running from northeast to southwest. Multiple reflections within the detector also broaden the PSF (Argyriou et al. 2023a; Law et al. 2023). The MIRI/MRS continuum reveals three distinct sources in NGC 5253 within the MIRI/MRS footprint, and a less distinct fourth. These can be seen most clearly in Figure 5, which shows images constructed from the 1L cube at 7μm as contours overlaid on visible and submillimeter images.

Figure 5 shows that the dominant IR continuum emission arises from the compact, luminous supernebula core within a dust lane visible in the HST 814W and in the 656N (Hα) filters. The dominant infrared source is coincident wih the radio core (Alonso-Herrero et al. 2004; Cohen et al. 2018). We call this source NGC5253-D1 ("D1"). Plumes of emission emerging from this central source are visible both in continuum and H α, as well as in the F555M filter. They also appear in the JWST continuum images, although unfortunately coinciding with the "petals" of the PSF. A second pointlike IR source, NGC 5253-D2 ("D2"), is clearly visible in the 814 continuum and Hα images to the northwest of D1. It is actually a very luminous H II region. The third distinct source, NGC 5253-D6, located ~ 50 pc to the southwest of D1, is more extended and diffuse.

h

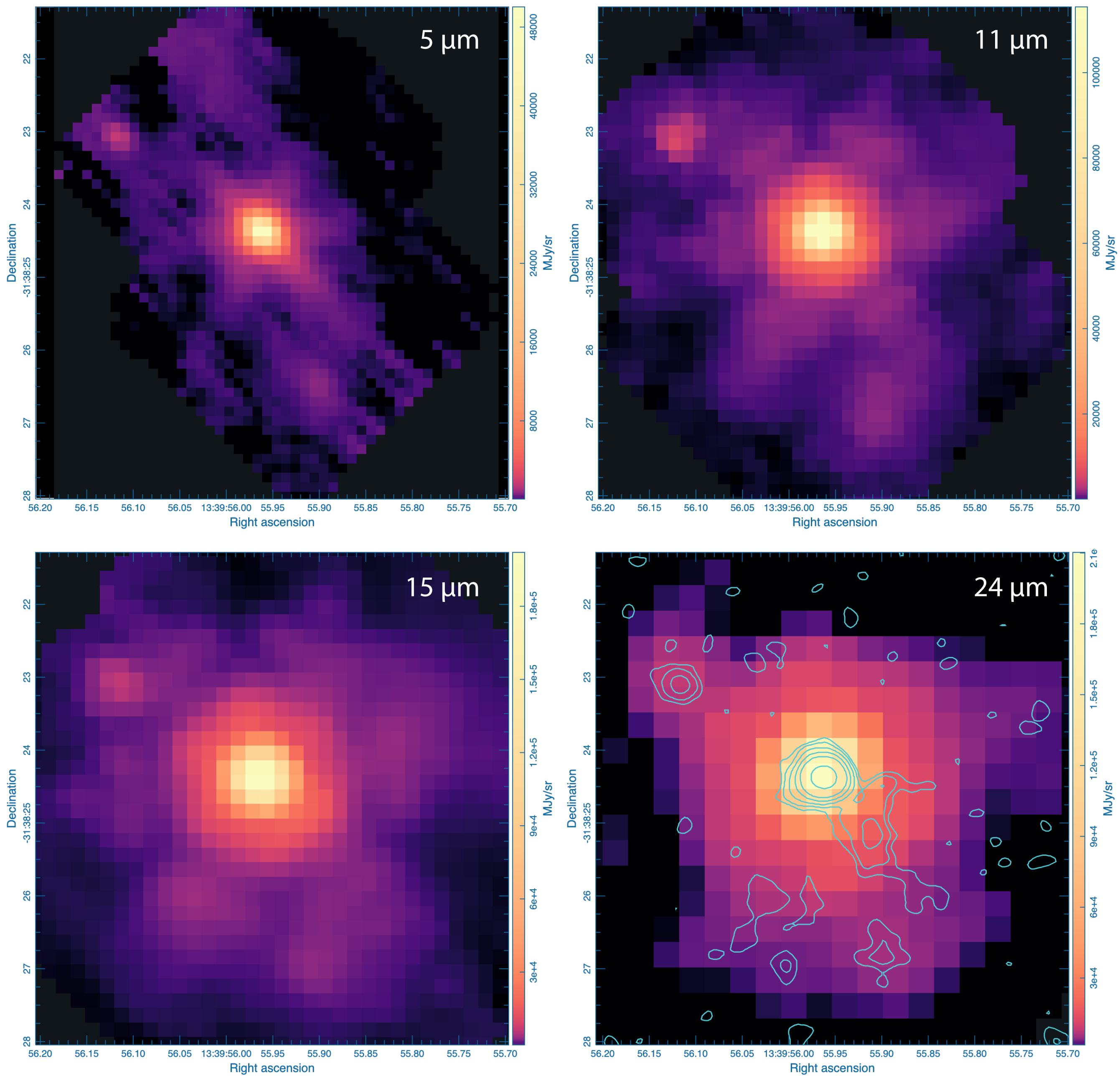

Figure 4. MIRI-MRS continuum images. (Top left): 4.95-5.0μm. (Top right): 10.6-10.8μm. (Bottom left): 14.7-15.0μm. (Bottom right): 23.8-24.3μm. Contours in this panel are $0\farcs3$ resolution 870μm ALMA continuum (Turner et al. 2017; Consiglio et al. 2017).

The fourth source NGC 5253-D4 ("D4") is less distinct and and can be seen most clearly by comparison with submillimeter and CO images in Figure 6. In NGC 5253, the 870μm continuum is a combination of free-free and dust. D4 is also associated with a CO cloud, which lies 15 pc ($\sim 0.9''$) and 15km s^{-1} away from the D1 cloud. Cloud D4 differs from other sources within the region in that its 870μm emission is dominated by dust, not free-free emission (Consiglio et al. 2017). Unfortunately, Cloud D4 lies along the "cruciform" artifact of MIRI/MRS (Fig. 4), appearing

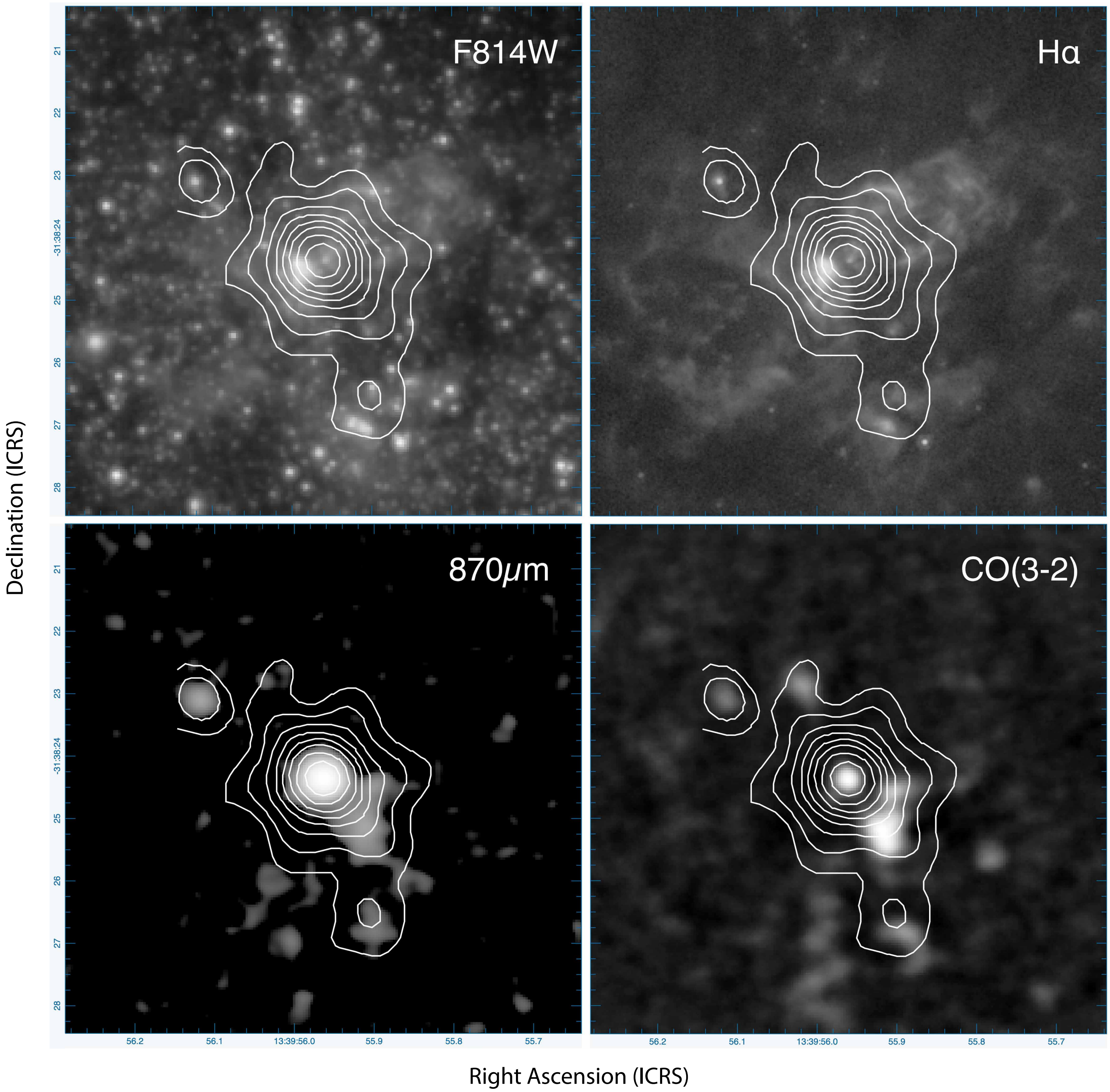

Figure 5. JWST 7μm continuum contours, with levels of 400, 600, plus $2^{(n-1)}$x1000 MJy/sr. Peak 1.24×10^5 MJy/sr. These are overlaid on: *(Top left):* HST/ACS F814W; *(Top right):* HST/ACS F656N ("Hα"); *(Bottom left):* ALMA 870μm continuum; *(Bottom right):* ALMA CO(3-2) integrated intensity.

as an extension of the central continuum source, D1; it cannot be cleanly separated spatially due to the dominance of D1. Even so, D4 is sufficiently offset that its spectrum differs significantly from that of D1.

3.3. *Mid-Infrared Continuum Regions and Spectra*

The starburst in NGC 5253 is of particular interest because it has an exceedingly luminous cluster, $L \sim 10^9$ $L_\odot$, within an exceedingly small volume, $r \lesssim$ 2-3 pc. The radiation field is intense and probably hard. What are the effects of this radiation field on dust, particularly small dust radiating in the mid-infrared? How far do these effects extend from the central cluster, NGC 5253-D1?

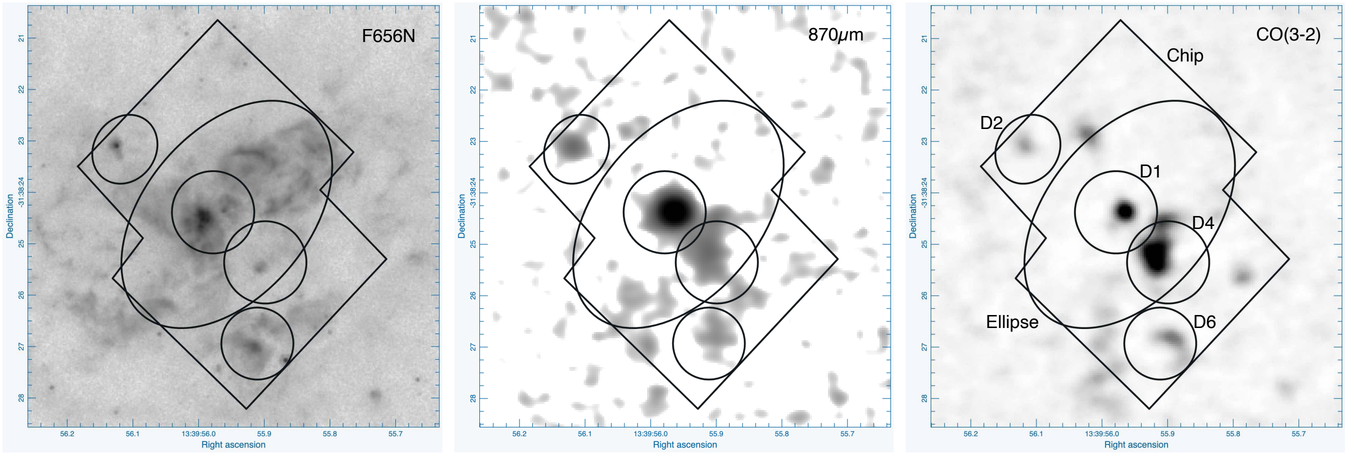

Figure 6. Regions for spectral extraction. Coordinates are ICRS; HST images are corrected using Gaia stars (Cohen et al. 2018). *(Top left):* HST/ACS F555M. Region D1 encompasses both the radio core and brightest optical source. *(Top right):* HST/HRC Hα. Ionized plumes extending to northeast and southwest are captured in the "Ellipse". *(Bottom left):* ALMA 870μm emission. Mostly free-free emission; the D4 region has significant submm dust emission. *(Bottom right):* ALMA CO(3-2) emission with regions and named CO clouds (Consiglio et al. 2017).

In the previous section we used the MIR continuum and the ALMA CO(3–2) map to define individual star-forming sources. We now describe how we determined apertures, or regions, from which spectra were extracted. Since all star-forming regions within this 100 pc MIRI/MRS footprint initially had the same metallicity and general host environment, spectral differences among the regions can be attributed to differences in stellar populations and conditions within the individual H II regions. Only the spatial resolution of JWST allows us to isolate individual H II regions and detect the spectral differences among them at the 3.7 Mpc distance of NGC 5253.

As discussed in §2, a pixel-by-pixel spectral analysis directly from the cubes is not possible because of spatial artifacts and strong spectral fringing due to the very bright central continuum source. Procedures for defringing spectra (Gasman et al. 2023) work best on 1D spectra rather than cubes. Thus apertures, or spectral "regions", were defined. We chose the sizes of the regions according to the recommendation that spectra be extracted from regions with radius $>$ 1.5 times the PSF FWHM (Law et al. 2023), while as much as possible avoiding spatial confusion. Since most lines of interest were at wavelengths shorter than 20μm, we aimed at $0\farcs8$, which is twice the PSF at 20μm (Argyriou et al. 2023a). For these apertures, photometric errors due to various effects on the PSF are $\lesssim$ a few percent. Regions near the edges of the chip have slightly smaller radii. At 3.7 Mpc, $0\farcs8$ corresponds to 15 pc, so the regions are about three times the size of the Great Nebula in Orion.

Regions were assigned to the MIR 5μm continuum sources D1, D2, and D6 (Fig. 5), to D4, to an extended region covering the H α plumes of the supernebula ("Ellipse"), and the entire 5μm footprint ("Chip"). The regions are shown in Figure 6. An additional region, "Chip minus D1" was defined as a region including all but D1. Region names beginning with "D" are named for molecular clouds, as identified in ALMA CO(3-2) maps of similar spatial resolution to JWST (Meier et al. 2002; Consiglio et al. 2017). Although they bear CO names, the spectral regions are not centered on the CO centroids. In particular, the region associated with the dominant source D1, associated with a CO cloud $\lesssim 0.3''(r < 3$ pc) in size, was drawn to include the brightest optical knot, "Cluster 5". Spectral region D4 is difficult to see in the JWST continuum because of its proximity to the cruciform artifact, so the CO image was used to define it. The D1 and D4 spectral regions overlap somewhat. D2 is near the chip edge, so its extraction region was slightly reduced, as was the case for D6. Details of the region sizes and centers are given in §5.

The MIRI/MRS spectra for the individual regions are shown in Figure 7. Color distinguishes the 12 spectral bands of MIRI/MRS. There are mismatches in continuum level between bands, but aside from D4, these are all much less than $\lesssim$ 5%. In D4, the mismatches in Channel 4 are 5-15%, with the larger mismatches beyond 15μm. We do not correct for the mismatches. Continuum emission is detected from 5μm though 25μm in all regions, when the detector response begins to degrade.

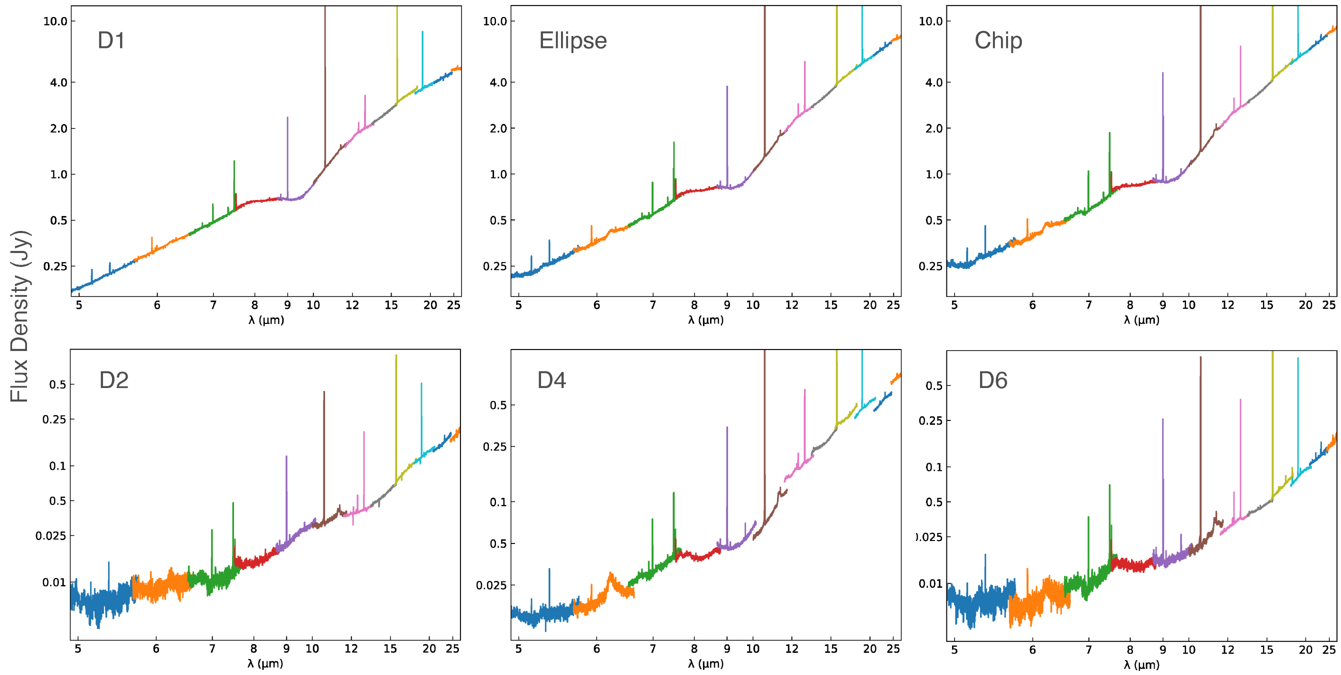

Figure 7. JWST MIRI/MRS continuum spectra for the spectral regions, from 1D defringed spectra. D1 dominates the larger Ellipse and Chip regions, shown on the top row. D1 shows a distinct 9.7μm silicate absorption feature, as do Ellipse and Chip. D2, D4, and D6 are far weaker. All regions show weak PAH emission, which is strongest in D4 and D6. The 6μm feature is particularly strong in D4. D2 has a weak 9.7μm silicate emission feature (§ 3.7.1.

The spectra have some features in common with Galactic H II regions. As in Galactic regions, the emission at 5 and 7μm is from very small grains (VSG), probably stochastically heated. Emission from classical large grains causes a rise in the spectrum beyond 10μm. The spectrum of D1 (and perhaps D2) seem to turn over at $\lambda \sim 20\mu$m. This is also seen in the ISO spectrum of the Trapezium region in Orion (Cesarsky et al. 2000). Degradation of the chip performance at the longest wavelengths and the possibility of broad, weak silicate absorption at 18μm make it difficult to quantify this effect.

The spectra also differ significantly from Galactic H II regions, in part because of the low metallicity of NGC 5253 and in part due to the extreme radiation fields of D1. The mid-infrared spectra of Galactic H II regions such as Orion or W49 are dominated by broad line features from large molecular structures such as polycyclic aromatic hydrocarbons (PAHs) (Cesarsky et al. 2000; Stock et al. 2014; Chown et al. 2024). Solid state features have been long known to be weak in high radiation, high intensity, and low metallicity environments such as NGC 5253 (e.g., Spoon et al. 2007; Lai et al. 2020). PAH features are present in all the regions, including D1 where the radiation is most intense. However they are very weak everywhere, even in regions far from D1. We discuss PAH emission in §3.7.2.

The 9.7μm silicate solid-state feature is present in some regions, but not all. Silicate absorption feature is clearly present in D1, as well as in the extended Chip and Ellipse regions dominated by D1, as expected based on the extinction. We discuss the silicate features in §3.7.1.

3.4. *Mid-Infrared Continuum Fluxes and Spectral Indices*

In Table 1 we present flux densities and mid-IR luminosities at representative wavelengths for the regions. The wavelengths are chosen to be relatively free of PAH emission to facilitate comparisons with other H II regions that have stronger PAH emission. Fluxes were measured from the 1D spectra for the spectral regions using CARTA. Values presented in the Table were interpolated from the loess-smoothed spectra to the specified wavelengths in R, as described in §2.

The total Chip fluxes can be compared to previous ground-based observations, with similar apertures, as compiled in Vanzi & Sauvage (2004). Ground-based fluxes at 12μm range from 1.67 to 1.9 Jy, with apertures of 4-7″; the JWST

Table 1. NGC 5253 Mid-infrared Continuum Properties

Region[a]	2.8 mm	5.0μ	7.0μ	15.0μ	20.0μ	α_5^{15}	α_7^{15}	α_5^{20}	α_7^{20}	$\log Q_0^c$	L_{OB}^d	L_{MIR}^e	$L_{MIR}^{est\ f}$
	Flux Density, S_ν^b					Spectral Index, $S \propto \nu^\alpha$							
	(mJy)	(mJy)	(mJy)	(mJy)	(mJy)						10^7 L$_\odot$	10^7 L$_\odot$	10^7 L$_\odot$
D1	27	180	480	2700	3800	-2.5	-2.3	-2.2	-2.0	52.69	100	36	55
D2	0.74	7.3	9.6	63	134	-0.8	-1.1	-1.0	-1.3	51.12	2.6	0.7	1.1
D4	0.94	15	30	300	530	-1.4	-1.2	-1.2	-1.1	51.23	3.4	3.4	5.2
D6	0.49	7.4	9.0	48	95	-0.6	-0.7	-0.7	-0.8	50.94	1.7	0.8	1.2
Ellipse	30.5	219	546	3510	5740	-1.5	-1.1	-1.3	-1.0	52.74	110	42	65
Chip-D1	5.2	76	97	1120	2430	-1.0	-1.3	-1.2	-1.4	51.97	19	16	25
Chip	32.0	256	578	3780	626	-1.0	-1.0	-1.0	-1.0	52.76	115	47	72

NOTE— [a] Coordinates of aperture regions are given in §5, and shown in Figure 6. [b]Flux densities are interpolated to the specified wavelength from loess-smoothed spectra. Uncertainties are $\lesssim$ 5%, except $\sim$ 10% for D2 and D6 at 5 and 7μm, see §2. Uncertainties in ALMA 2.8cm fluxes are $\sim$ 5%. [c]Q_0 are from 2.8 cm fluxes for 10^4 K gas using $Q_{50}(s^{-1}) = 1.31\nu_{11}^{0.118}$ $D_{\rm Mpc}^2$ S_{100} (mJy). Units of Q_{50} are 10^{50} s^{-1}. [d]L_{OB} is the predicted O star luminosity based on the Q_0 using $\log(L/L_\odot/Q_{50}/s^{-1}) = -43.7$ (Turner et al. 2017), based on Starburst99 models for a 1 Myr, z=0.008 cluster with upper mass cutoff of 120M$_\odot$(Leitherer et al. 1999). [e]Observed luminosity directly summed from line-free continuum spectra. [f]L_{MIR}^{est} corrects observed luminosities to account for the Rayleigh-Jeans tail of the warm MIR dust, assuming peak wavelength of 20μm and β=1.7.

value is 2.3±00.2 Jy. Some of this variation is due to differing filter responses. Fluxes at 20μm range from 3.7-6.1 Jy for apertures of 6–8″, respectively; the JWST value is 6.3±0.6 Jy. The only direct comparison of ground-based fluxes that can be made for the D1 region alone is to the high resolution ($\sim 0.3''$) Keck/Long Wavelength Spectrometer images of Gorjian et al. (2001). They measured 2.2 Jy at 11.7μm, whereas JWST finds 2.1±0.2 Jy, and for the Keck/LWS value of 2.9 Jy at 18.7μm, the MIRI flux is 3.6±0.4 Jy. The fluxes are consistent within the uncertainties. They also demonstrate the importance of high resolution for the accurate characterization of extragalactic H II regions.

To compare different sections of the MIR continuum, we have computed spectral indices, α ($\propto \nu^\alpha$). There is a distinct change in the continuum evident such that the dust below $\sim$ 10 μm is flatter than the rising spectrum beyond $\sim$ 10 μm. The dust spectrum below 10μm is dominated by VSGs, stochastically heated. The longer wavelength radiation tends to be dust heated by intense radiation fields from these luminous clusters, although large nanoparticles with $10^3 - 10^4$ C atoms that are stochastically heated can also in theory produce radiation even at these wavelengths (Draine et al. 2021). To characterize the different contributions of VSG and classic dust, we compute spectral indices, α, in clean parts of the spectrum between the longer wavelength spectral regions at the wavelengths chosen. These spectral indices are listed in Table 1, for fluxes at wavelengths of 5μm, 7μm, 15μm, and 20μm.

Most regions have spectral indices of $\alpha \sim -1.0$. However, D1 has a significantly steeper spectrum, with $\alpha \sim$ -2 to -2.5. The emission from D1 is dominated by the longer wavelengths, 15-20μm, rather than by the VSGs emitting at the shorter wavelengths. Comparison of the Ellipse and Chip regions, which contain D1, show that as the aperture increases, the contributions of VSG likewise increase. For comparison, the Trapezium region of Orion (Cesarsky et al. 2000) has a similar index to D1, slightly flatter, with values of $\alpha \sim$ -1.8 to -2.3. We note in particular the region "Chip-D1", which includes everything in "Chip" except (minus) D1. Chip-D1 includes D2, D4, D6, and all extended emission. This region also has the same relatively flat values as the smaller H II regions but also the much more diffuse D6. In summary, the VSG contribution is relatively larger in the extended region outside of D1 than it is within D1, and this is reflected in D1's steeper spectral index.

The flatter spectra for the more extended components in NGC 5253 may indicate conditions within the region, as described by dust models. It is convenient to characterize the radiation field by U, energy density in units of the standard Galactic interstellar radiation field (ISRF Mathis et al. 1983); $U = 1$ being the Milky Way ISRF, and typical H II regions having $U \sim 10^5 - 10^6$ at the faces of PDRs. Models of dust emission suggest that these lower spectral indices are consistent with spectra of lower excitation parameter, $U \lesssim 10^2 - 10^3$ for the predicted emission spectra of Draine & Li (2007). The lower spectral indices may also indicate increasing PAH fraction (Draine & Li 2007), which in turn may also be related to the radiation field, since the lower spectral indices are seen in regions away from D1. It is likely that the VSG population in D1 is suppressed. Because of the high and variable extinction it is difficult to predict values of the radiation within the region, and the VSGs may be a guide to the variation of U.

The luminous and pointlike H II region D2 also shows the lower values of spectral index than D1, values similar to the extended emission. Although D2 is a luminous H II region it may be more evolved than D1, since it is visible, although very compact in H α (Fig. 5) It may perhaps have undergone structural changes such as the development of an expanding shell or champagne flow, as seen in Galactic H II regions (Wood & Churchwell 1989), so that the dust-heating radiation field is less intense. As a lower luminosity H II region it also has fewer ionizing stars, and possibly a softer radiation field.

3.5. *The Ratio of Mid-infrared to Radio Continuum Flux*

Free-free fluxes are also listed in Table 1 for the spectral regions. These were measured from 107 GHz (2.8 mm) ALMA maps ($0\farcs5$ resolution, ALMA Project 2013.1.00833.S, P.I. E. Rosolovsky). At $\lambda = 2.8$ mm, the emission is all free-free emission, with negligible contributions from dust or synchroton emission. The largest angular scale of these images is $4''$, which is close to the JWST chip size, so missing flux from short baselines is not an issue. From the free-free flux we derive extinction-free Lyman continuum rates, which are also given in Table 1. We note that the extinction in the MIR is not insignificant for D1; this is discussed further in (Beck et al. 2025).

The total Lyman continuum rate for the D1 supernebula core is $\log(\mathrm{Q_0}) = 52.68$, while the entire Chip region has $\log(\mathrm{Q_0}) = 52.76$. This can be compared to radio recombination line estimates for the D1 source of $\log(\mathrm{Q_0}) \sim 52.30-52.5$ $(\mathrm{D}/3.7\ \mathrm{Mpc})^2$ (Mohan et al. 2001; Rodríguez-Rico et al. 2007; Bendo et al. 2017). The Q_0 value for the entire Chip is consistent with that predicted by VLA and ALMA studies (Turner et al. 1998; Rodríguez-Rico et al. 2007; Bendo et al. 2017).

The continuum spectra allow us to compute the ratio of MIR to free-free flux for the H II regions in NGC 5253. The excellent spatial correlation of free-free and MIR dust emission within Galactic H II regions has long been known (e.g., Genzel et al. 1982). The predictable relation of MIR and free-free flux is an important diagnostic of O star formation, and this relation has been used previously in NGC 5253 to argue that the luminous D1 is most likely an H II region and not an AGN (Gorjian 1996). The high spatial resolution of JWST allows individual H II regions to be isolated so that the relation can be studied in other galaxies.

We obtain ratios of $S_{20\mu m}/S_{2.8mm} = 140$, 180, and 190 for regions D1, D2, and D6, respectively, and 190-200 for Ellipse and Chip. This can be compared to the values seen in W51 of $S_{20\mu m}/S_{6cm} \sim 100$ (Genzel et al. 1982), which, translated to 2.8mm, would be a ratio of 140. The agreement between the Galactic H II value and that measured in NGC 5253 is excellent.

At first glance it seems surprising that the MIR/radio ratio in these low metallicity H II regions is the same as those in the Galaxy, since one might expect the gas-to-dust ratio, and thus the flux, to scale with metallicity. However, the bulk of the dust heating is due to Lyman α absorption by dust, which may not be as sensitive to metallicity, so long as there is sufficient dust to capture these high optical depth photons. The moderately low metallicity of NGC 5253 apparently does not change the fact that the Lyman α photons will tend to end up on dust within the H II region.

3.6. *Mid-Infrared Luminosities and Photon Escape in NGC 5253*

Observed MIR luminosities, $\mathrm{L_{MIR}}$, are computed from the observed spectra and are listed in Table 1. These fluxes correspond only to the measured fluxes in the 4.9-28μm spectral range, not beyond, and thus are an underestimate of the luminosity emitted by "warm" dust. We correct for the Rayleigh-Jeans tail of the distribution of the flux represented here by modeling the spectrum as a modified blackbody with peak emission up to 20μm, similar to the peak in Orion (Cesarsky et al. 2000). We assume an emissivity $\beta \sim \nu^{1.7}$. For these parameters the Rayleigh-Jeans tail contributes ∼35%. The extrapolated blackbody luminosities are listed as L_{MIR}^{est}; these are still underestimates since they do not include the power by dust with peak emission at longer wavelengths, the "cold" dust (e.g. Rémy-Ruyer et al. 2013, 2015). From the Lyman continuum rates, $\mathrm{Q_0}$, we predict a corresponding luminosity due to star formation, designated as L_{OB} based on STARBURST99 models ($\mathrm{Z}=0.008\mathrm{Z}_\odot$, mass cutoffs 1 and 150 $\mathrm{M}_\odot$, continuous star formation, age=1 Myr).

There are two potential corrections to be made to the radio fluxes. Radio free-free emission is affected by dust, since the dust directly competes with gas for ionizing photons. Given IR luminosities, it is possible to correct for the effects of direct absorption of UV by dust, accounting for the fraction of dust heated by Lyman α photons. This process is described by Inoue (Inoue 2001; Inoue et al. 2001). Using their curve for the LMC for average dust absorption efficiency, ϵ, we adopt a value of unity, since $A_V \gtrsim 15$. From the values in Table 1, using $\mathrm{L_{MIR}^{est}}$ for the luminosity, we obtain a fraction, f, of ionizing to total UV photons of $f \sim 1.06$ for D1. In other words, there is negligible direct absorption of UV photons by dust within the D1 H II region; the observed dust emission is due to Lyman α trapping. The computation changes little, $f = 1.01$, for the values for the entire Chip region. For comparison, typical values for Galactic H II regions are $f \sim 0.3$ (Inoue et al. 2001). So we do not have to correct for direct absorption of UV by dust within the D1 H II region.

The second potential correction to the radio flux is for UV photons escaping beyond D1 and beyond Chip. Comparing the free-free fluxes of D1 and Chip suggests that most of the ionizing flux within the central 100 pc region has its origin in D1. The free-free flux from D1 is $\sim 90\%$ of the total free-free flux within Ellipse, and 83% of the flux within Chip, which contains other H II regions. The Ellipse region has visible plumes of nebular emission, as can be seen in Figure 5. Beyond the 100 pc region covered by Chip, VLA continuum observations at 33 GHz predict a flux at 107 GHz of $\sim$ 40-42 mJy, as compared with 32 mJy observed within the Chip region. If these photons arise within D1, then $\sim$25% of photons escape beyond the MIRI/MRS chip.

The MIRI/MRS fluxes and luminosities of Table 1 are consistent with the photon escape picture. The MIR should account for most of the IR luminosity from these H II regions (e.g., Peeters et al. 2002). From Table 1 it can be seen that the estimated total luminosity emitted by mid-infrared dust is less than that predicted from radio free-free emission. A little over half the estimated star-forming luminosity within D1 is reflected in MIR dust emission within D1 itself. Roughly 70% of the luminosity generated by the cluster within D1 is reradiated in the MIR. This is consistent with the fraction of radio free-free emission confined to D1, within the inner arcsecond, and the larger region (Turner et al. 1998; Rodríguez-Rico et al. 2007). A substantial luminosity, $L \sim 3 \times 10^8$ $L_\odot$, emerges from the 100 pc Chip region in some form other than MIR emission.

We conclude, based on the comparison of the luminosities implied by the mid-IR emission and the radio free-free fluxes, that at least $\sim 25\%$, of the UV photons are escaping from the $r \sim 15$pc D1 aperture, even though the extinction along the line of sight is high ($A_v \gtrsim 15$). Photons can escape if the D1 cluster/cloud is porous. These escaping photons are absorbed by dust out beyond a radius of 50-60 pc from D1.

3.7. *Solid State Features in the NGC 5253 Starburst*

NGC 5253 has a relatively low metallicity, $Z \sim 0.3$ $Z_\odot$ and an incredibly luminous, embedded young cluster. Both factors work against seeing spectral features from solid particles or large molecules, including large hydrocarbon molecules such as PAHs. However, NGC 5253 also has a high extinction and dense molecular clouds, including molecular gas within the $r < 3$pc D1 core. So there is clearly a significant dust presence and therefore possibly also very large molecular structures such as PAHs.

As shown the continuum spectra of Figure 7, weak solid state features appear in all the spectra. We discuss first the 9.7μm silicate feature.

3.7.1. *Silicate Feature: Absorption and Emission*

The very broad feature centered at $\sim 9.7\mu$m has traditionally be associated with astronomical silicates, with recent supporting evidence in favor of this interpretation (Gordon et al. 2023). We detect the silicate feature in NGC 5253 for the first time. We present plots of the silicate feature in the different regions in Figure 8. The 9.7μm feature is strongest in D1, as well as the Ellipse and Chip regions dominated by D1.

We calculate optical depths for the silicate feature following the method of Spoon et al. (2007), with slight modifications. In this method, a power law continuum is fit between 5.5μm and 14.5μm and used to predict a value at 9.8μm; $\tau_{9.7}$ is defined as the natural log of the ratio of observed to predicted flux. The wavelength ranges, 4.9-6.0μm and 14.5-15.0μm, were used to fit a power law and also a second order polynomial to the continuum. In addition, following the suggestion of Brandl et al. (2006), we extended the fit to longer wavelengths, 18-23μm, which required a fourth order polynomial. The 3S band, which appears to be offset relative to other bands, was omitted from the fit (the very strong [Ne III] line is at the lower edge of the band). The fourth order polynomial is a very good fit to the data out to 25μm, reflecting the turnover in the spectrum at longer wavelengths. The fits are shown in Figure 8, and the resulting $\tau_{9.7}$ are given in Table 2.

Region D1, the supernebula core, has the strongest 9.7μm feature. Of the three fits shown in Figure 8, the fourth order polynomial gives the largest value $\tau_{9.7}$= 0.41 for D1. While the fourth order polynomial fits the longer wavelengths, there is no reason a priori that it should be preferred for wavelengths near 10μm. The power law fit gives the smallest value, $\tau_{9.7}$= 0.21, and the second order polynomial value is $\tau_{9.7} = 0.32$. Given that the uncertainty depends entirely on the assumed functional fit, we take the median value corresponding to the second order polynomial fit, giving $\tau_{9/7} = 0.3 \pm 0.1$ for D1.

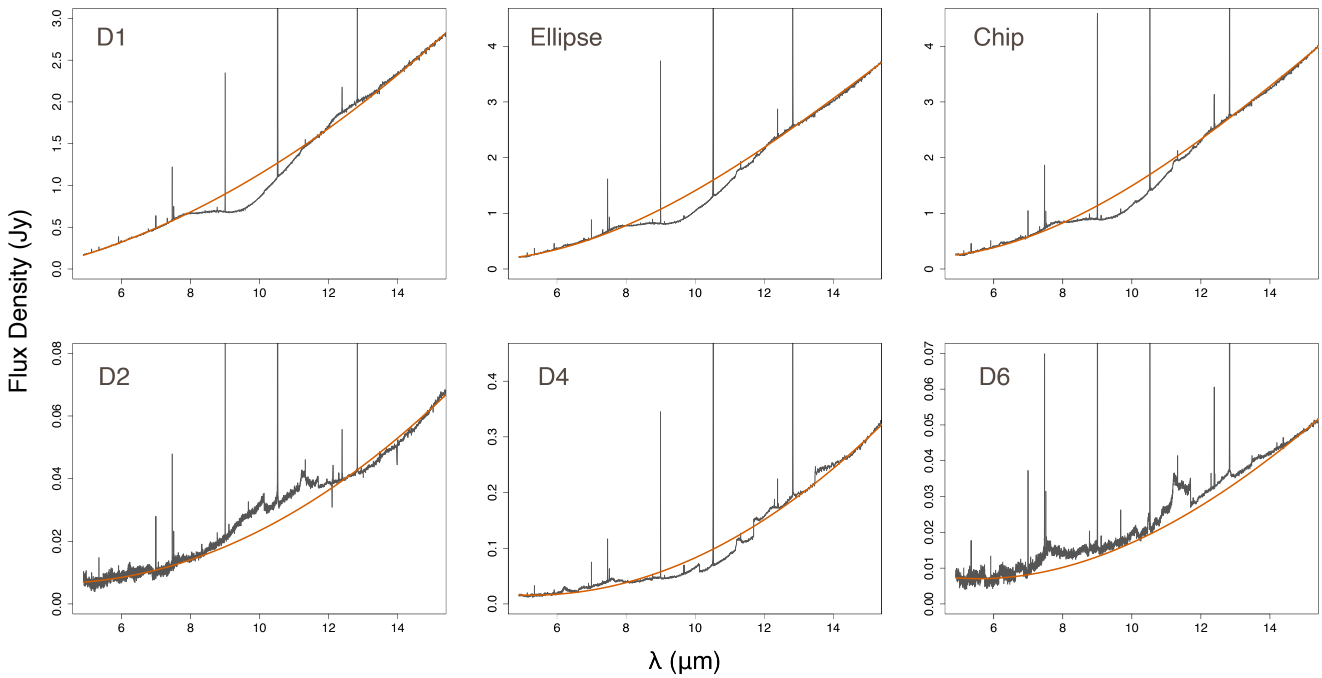

Figure 8. Fits to the 9.7μm silicate feature in the regions. Shown is a second order polynomial fit to the continuum from 5.0-5.5μm and 14.3-14.5μm.

In D2 the silicate feature appears in emission. Silicate emission is typically observed toward evolved stars, but it has also been observed in a few H II regions, including the Trapezium region in Orion, in NGC 3603, and in the LMC sources NGC 346 and N66B (Cesarsky et al. 2000; Lebouteiller et al. 2007; Whelan et al. 2013). D2 appears as a bright, point-like ($\lesssim 0\farcs2$) source of Hα emission (Fig. 6). Since silicate emission is relatively rare in H II regions, although commonly observed in younger protostars and evolved stars, Whelan et al. (2013) suggest that it is an indicator of a very brief phase of cluster evolution. Since D2 has a visible H II region and also a closely associated molecular cloud, it is likely of moderate age, possibly older than D1.

In D6 the spectrum nominally suggests faint silicate emission, but it is also consistent with zero or faint absorption. The presence of CO emission, dust lanes, and submillimeter continuum emission suggests that dust is present in D6, but the continuum is weak so it is difficult to draw conclusions.

The Chip and Ellipse regions are dominated by D1, but the silicate absorption is less distinct than it is in the undiluted D1 spectrum.

The corresponding silicate feature at 18.7μm is observed in Galactic sources (Gibb et al. 2004). This feature is less deep than the 9.7μm and very broad (Chiar & Tielens 2006). We do not see evidence of the 18.7μm feature in the spectra of NGC 5253, but this is not surprising given its broad and weak profile; it is half to one third the optical depth of the 9.7μm feature. It is also not evident in the Spitzer spectra of Beirão et al. (2006); the continuous spectrum in their central position is relatively featureless between 10 and 20μm aside from the 11.3μm PAH feature.

The silicate feature in D1 is relatively weak for the estimated extinction toward this source, $A_V \gtrsim 15$. In Galactic regions, the optical depth of the 9.7μm silicate feature is related to extinction by the empirical relation $A_V/\tau_{9.7} = 18.4 \pm 1.0$ (Whittet 1992). The Galactic center region has anomalously low values for this ratio, and no clear relation is seen there (Gordon et al. 2023). In NGC 5253 the value of $A_V/\tau_{9.7} \sim 50 \pm 20$, higher than the Galactic prediction by factors of 3–5. This would be consistent with a trend toward weaker silicate absorption in lower metallicity environments.

There are a number of reasons why the silicate feature could be weaker than expected for the dust column based on the Galactic relation. One reason could be that there exist compact H II regions within D1 that have silicate emission, similar to D2, that dilute the absorption feature from the surrounding gas. There is evidence for substructure within

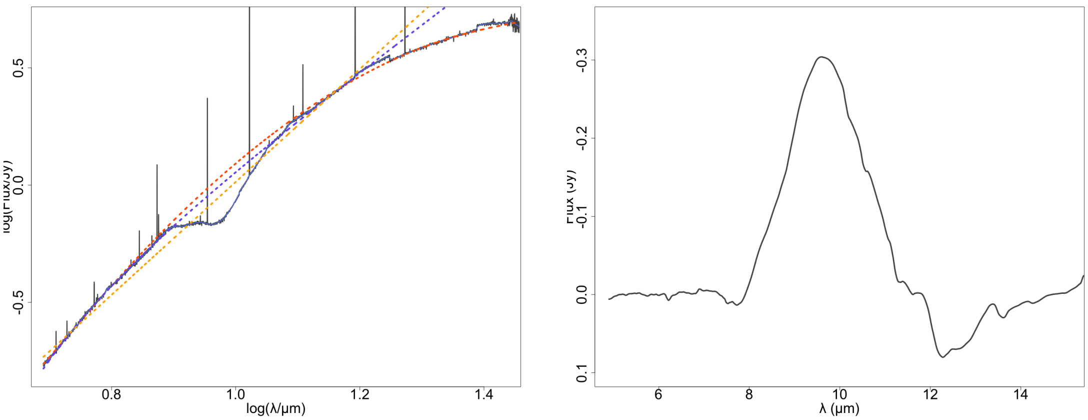

Figure 9. *(Left:* Fits used to determine the optical depth of the 9.7μm silicate feature in D1. The top line is a fourth order polynomial fit to the spectrum from 5.5 – 24μm; the middle line is a second order polynomial fit to 5.0-5.5 and 14.3-14.7 μm; the bottom line is a power law fit between 5.0-5.5 and 14.–14.7μm as specified by the Spoon model. *(Right): Silicate feature, based on subtraction of the second order polynomial fit from the observed loess-smoothed spectrum.*

D1, even within $r < 3$ pc (Turner et al. 2017). Another possible explanation is that the dust in the region has a higher percentage of carbonaceous dust relative to silicate dust than is typical for Galactic H II regions.

3.7.2. *PAH Features*

The distinctive 6.2μm and 11.3μm features were seen in all regions. PAH emission can be weak in the presence of intense or hard radiation fields (Hunt et al. 2010) and also in low metallicity galaxies (Lai et al. 2020). NGC 5253 has both conditions: low metallicity and intense radiation fields. Given that these regions all lie within a small section of the galaxy, differences in their spectra should be due to local conditions, such as radiation field intensity or hardness, and not host metallicity.

A complete treatment of PAH features would include features at wavelengths shorter than those detected by MIRI/MRS, such as the 3μm feature. Such a treatment is beyond the scope of this paper. However, we can discuss some of the features that are detected with MIRI/MRS and their variation among regions of differing luminosity.

PAH features appeared in the spectra at 5.3, 6.2, 7.6, 8.6, and 11.3μm. A sixth feature, at 5.7μm, was seen weakly in one region, D4. To quantify these features, we measured fluxes and equivalent widths from the 1D spectrum using Specviz, and the fluxes and equivalent widths are given in Table 2. We fit a linear baseline to the features, similar to the clip method employed by Draine et al. (2021).

The features at 7.6μm and 8.6μm are difficult to separate with a simple linear baseline; there is likely to be a"plateau" feature peaking under them (Peeters et al. 2004; Brandl et al. 2006; Chown et al. 2024) that may dominate the equivalent widths. There is also the the broad 9.7μm silicate feature to one side. The instrumental response also complicates the measurement of fluxes since the 7.6μm and 8.6μm PAH features straddle the bands. Since we cannot separate the features, we present only fluxes from 7-9μm, which includes both features and the underlying plateau, to allow basic comparisons of the different regions.

We do not detect the 7.6μm and 8.6μm features in H II regions D1, D2, and Ellipse. Because of the rapidly changing spectrum in this region due to the silicate feature, which is seen in all three regions, it is difficult to assign upper limits without a detailed model of PAHs and silicates. We note that all three regions in which 7.6 and 8.6μm are absent have a strong H II region character, with free-free emission, H α, and other nebular emission (Paper II). The other regions, D4, D6, Chip-D1 and Chip, have equivalent widths of 0.2-0.5 μm, significantly higher than those of the H II sources, suggesting a substantial contribution from the plateau.

The 6.2μm and 11.3 μm features are seen in all regions. In D1 and D2 these are the only PAH features clearly detected. They are most prominent in region D4, in spite of strong spectral fringing in this region. Equivalent widths for the 6.3μm feature range from 0.002 in D1, to 0.08, four times higher, in D4 and D6. For the 11.3μm feature, equivalent widths are EW $\sim .005 - .05.\mu$m, largest in D6. The ratio of 6.2/11.3 fluxes is also given in Table 2; it is roughly unity for the sources. The exceptions are D1, in which the 6.2μm feature is half as strong as the 11μm

Table 2. NGC 5253 Broad Mid-Infrared Spectral Features

Region	$\tau^a_{9.8}$	14 μm[b]	5.3 μm[c]		6.2 μm[c]		7.8 μm[c]		11.3 μm[c]		6.2/11.3	PAH[d]/14μm
		Flux	Flux	EW	Flux	EW	Flux	EW	Flux	EW		
		W m^2	W m^2	μm	W m^2	μm	W m^2	μm	W m^2	μm		
D1	0.3(0.1)	3.6e-14	...	...	6.2e-17	.0022	...	...	1.6e-16	0.0047	0.4	0.006
D2	−0.3(0.15)	8.0e-16	...	...	2.0e-17	.028	...	...	2.3e-17	0.027	0.9	0.05
D4	0.3(0.06)	3.8e-15	6.4e-18	0.0041	1.2e-16	.079	3.3e-16	0.17	6.8e-17	0.028	1.8	0.14
D6	−0.1(0.03)	6.4e-16	1.1e-17	0.017	4.3e-17	0.081	2.4e-16	0.45	3.3e-17	0.049	1.3	0.5
Ellipse	0.3(0.05)	4.6e-14	2.6e-17	0.001	3.4e-16	0.011	...	...	3.8e-16	0.0010	0.9	0.02
Chip-D1	−0.12(0.15)	1.4e-14	7.8e-17	0.011	3.7e-16	0.059	2.9e-15	0.44	3.3e-16	0.033	1.1	0.26
Chip	0.3(0.04)	5.0e-14	1.1e-16	0.0038	5.4e-16	0.016	8.5e-15	0.25	5.9e-16	0.013	0.9	0.20

NOTE— [a] Optical depth of silicate feature as defined in text, with its uncertainty. [b] "14 micron" flux is measured from a 1μm wide band centered at 14.3μm. Uncertainties in PAH line fluxes are determined by baseline choice and are ∼10%. The "14 micron" flux is computed for a 1μm band centered at 14.3μm. Cutoffs for the feature fluxes are: 5.22-5.32μm; 6.1-6.5μm; 7-8.99μm; 11.1-11.5μm. Bright line emission was subtracted from the fluxes and EW. [d] "PAH" is the sum of the fluxes of the PAH features.

feature, and D4, in which it is twice as strong. While we have not separated the features at 7.6μm and 8.6μm we note that the relative strength of the 11.3μm feature compared to the 7-8μm features is consistent with the low silicate optical depth, based on analyses of other galaxies (Lai et al. 2020). The 6.2μm and 11.3μm features were also recently detected in the low metallicity starburst in II Zw 40 by Lai et al. (2025). II Zw 40 is a near twin to NGC 5253, in many respects; this may indicate that the 6.2μm and 11.3μm features are relatively robust in low metallicity starbursts.

We can put these in context by comparing to a local spiral with active nuclear star formation, IC 342, which has similar continuum fluxes, and a similar star formation rate to NGC 5253. For the PAH features at 6.2μm and 11.3μm, IC 342 has fluxes of 1.5×10^{-14} W m^{-2} and 1.8×19^{-14} W m^{-2}, with EW of 0.5 for both (Brandl et al. 2006). In comparison, NGC 5253-D1 has fluxes and equivalent widths that are 230 times weaker for the 6.2μm line and 100 times weaker for the 11.3μm line. Even in cloud D6, a weaker ($L \sim 10^7$ L$_\odot$) source which is at least 50 pc from the embedded D1, has a 6.3μm EW that is 25 times weaker, and 11.3μm EW that is 10 times weaker than those in IC 342, indicating that it is not just an effect of radiation field, but also the host metallicity. The harsh environment in NGC 5253 has a greater effect on the smaller grains producing the 6.2μm emission.

For a uniform comparison to continuum, we define a "14μm" flux, following (Lebouteiller et al. 2007), to be the continuum flux in the featureless region centered at 14.3μm of 1μm width. This flux is given in Table 2, and this flux is compared to the sum of the fluxes in the PAH features, which we designate "PAH". The overall value for the Chip is 0.2; values range from 0.006 in D1, to 0.5 in D6. This wide range of values reflects the fact that interstellar conditions must vary intensely over ∼ 10-20 pc spatial scales within this starburst.

The picture of PAHs within the NGC 5253 starburst is complex. The comparative lack of PAH emission within region D1 is expected, given that a luminosity of $\sim 10^9$ L$_\odot$ is contained within this 15 pc aperture, and only the most robust dust species will survive. Region D4, which is only ∼ 15 pc distant from D1, has some of the brightest PAH emission. The PAH emission in D4 may be tracing a PDR region at the periphery of the luminous D1 H II region; however, since the molecular cloud encasing D1 is smaller than the 15 pc separating D1 and D4, this requires the D1 molecular cloud to be porous. The other source of PAH emission comparable to D4 is D6, which is ∼ 50 pc from D1. In D6, in situ excitation of the PAHs by the H II region there would be required for their emission. More detailed modeling, including near-IR features, could reveal differences that could distinguish the different environments from which the PAH emission arises in D4 and D6.

4. DISCUSSION

The MIRI/MRS instrument on JWST allows us to probe deeply into the inner workings of a region of extreme star formation. It has revealed, in addition to the compact supernebula, NGC 5253-D1, known for its giant H II region and compact radio core, at least three additional H II regions within a radius of 50 pc. The regions differ in characteristics; the dominant D1 is 50 times more luminous than D2, which itself has a luminosity of 10^7 L$_\odot$. D6 is of similar luminosity to D2, but its MIR continuum and molecular morphology is much more irregular and dispersed than D2, and there is a visible cluster in D6.

The supernebula core, within region D1, is the dominant source of ultraviolet radiation within the central starburst region. It is powered by a cluster of at least 10^9 $L_\odot$ within a compact H II region, less than 2 pc in extent; radio free-free emission extended beyond the MIRI/MRS footprint suggests that the luminosity could be 25% higher than estimated here (Rodríguez-Rico et al. 2007). The impact of the cluster within D1 on its surroundings is, as yet, minimal. The cluster is encased in a CO cloud of radius <3 pc; the CO linewidth is narrow, 25 km s^{-1}, and reflects the cluster mass. The CO appears to be mixed in with the cluster, and a Gaussian linewidth points to clumps orbiting in the cluster potential. Indications are that D1 is not yet disrupting star formation within its pc-scale boundaries.

All four continuum sources within the central 100 pc have emission from VSG dust at wavelengths up to 9μm, as well as classical warm dust emission beyond 10μm. Spectral indices between fluxes at 5 and 7μm and fluxes at 15 and 20μm are all ~ -1 ($S \propto \nu^\alpha$), except for D1, which has a spectral index of $\sim 4-2.4$. D1 is dominated by dust emission at the longer MIR wavelengths, suggesting a relative paucity of VSG dust.

Emission from PAHs is seen in all regions, including faintly in D1. The PAH emission is relatively weak, as is often the case in low metallicity systems. However, the influence of high radiation fields can be seen. D1 has the weakest PAH emission, showing features only at 6.2μm and 11.3μm. D4, which is only 15 pc away, shows stronger PAH emission features, as does D6, although still very weak as compared to Galactic regions such as Orion (Chown et al. 2024). The H II region D2, like D1, is only detected in the 6.2 and 11.3μm features. These features appear to be more robust against intense radiation fields.

The PAH emission from D1 is particularly intriguing because there is bright CO(3-2) emission associated with D1 and kinematic evidence that the CO is mixed in with the star cluster. One might therefore expect PAH emission associated with PDRs within the cluster; it is seen but only very weakly.

The 9.7μm silicate feature appears in the spectra but is weaker than observed in Galactic H II regions (Chiar & Tielens 2006; Gordon et al. 2021; Gibb et al. 2004). The strongest 9.7μm absorption is in D1, which has the most intense radiation field. By contrast, the smaller H II region D2 shows the 9.7μm feature in emission; perhaps this is an evolutionary effect (e.g., Whelan et al. 2013), since D2 also has a visible compact Hα source (Fig. 6).

Finally, we note that, in spite of the high extinction in the region, there is evidence in the MIRI/MRS data for photon escape, including UV photon escape. On scales beyond the central 100 pc of the MIRI/MRS footprint, the radio fluxes from the central 30″ region are as high as 40-45 mJy (Rodríguez-Rico et al. 2007). This suggests that at least 25% of the UV photons escape the ∼15 pc diameter D1 region. HST images in the F658N (Fig. 6) and F555W filters (Fig. 3) show extended nebulosity around the location of the supernebula. From the curvature of the arcs, one might infer circumstantially that the nebulosity is driven by the central nebula, and that these plumes are due to UV photons escaping from D1. The ionization may extend out to ∼ 200-300 pc to the ionization sheath surrounding the infalling molecular streamer. This is unexpected given the high $A_V \gtrsim 15$ toward D1 (Turner et al. 2003; Alonso-Herrero et al. 2004). The HST images also clearly show dust lanes, which often correspond to CO features; they are an excellent indicator of the fine structure of the dust within the region.

5. INDIVIDUAL REGIONS

Below we discuss the individual regions from which spectra were extracted. Coordinates for D1, D2, D4, and D6 spectral extraction regions are given, as well as positions from the high resolution 1.3mm ALMA image of Figure 3. The 1.3mm peaks represent the bright cores of the H II regions. These coordinates are close, but not coincident, with the centers of the spectral regions shown in Figure 6 and listed in Table 1.

1) *Region D1, the core of the supernebula.* Region center: $13^h\ 39^m\ 55\overset{s}{.}962$, $-31°\ 38'\ 24\overset{''}{.}37$, aperture radius: $0\overset{''}{.}8$. The dominant MIR continuum source is the subarcsecond core of the "supernebula", located at $13^h\ 39^m\ 55\overset{s}{.}962$, $-31°\ 38'\ 24\overset{''}{.}37$ (1.3mm). Based on radio free-free and recombination line fluxes, its Lyman continuum rate is $Q_0 \sim 3\times10^{52}\ s^{-1}$ (Turner et al. 1998; Rodríguez-Rico et al. 2007; Bendo et al. 2017), corresponding to a large cluster with ∼1000 O stars. The CO cloud and dense core of the H II region are smaller than the spectral region defined here (Turner & Beck 2004; Turner et al. 2017). The CO emission in D1 coincides in both position and velocity with infrared and radio recombination line emission (Beck et al. 1996; Turner et al. 2003; Mohan et al. 2001; Rodríguez-Rico et al. 2007; Bendo et al. 2017; Cohen et al. 2018; Beck et al. 2020). The CO(3-2) emission is unusually hot and apparently optically thin (Consiglio et al. 2017). These peculiarities in the CO are strong evidence that the molecular gas in D1 is mixed in with the nebula within $r \lesssim 3$ pc ($0\overset{''}{.}2$). (Turner et al. 2017; Consiglio et al. 2017).

2) *Region D2, pointlike H II region, possible blister.* Region center: $13^h\ 39^m\ 56\overset{s}{.}107$, $-31^\circ\ 38'\ 23\overset{''}{.}16$; aperture semi-major axes: $0\overset{''}{.}8$ x $0\overset{''}{.}6$, p.a. 326. The pointlike H II region within D2 is located $2\overset{''}{.}3$ ($\sim$ 40 pc in projection) to the northeast from D1. It is very bright in the HST/NICMOS Paα image of Alonso-Herrero et al. (2004). The CO centroid is $13^h\ 39^m\ 56\overset{s}{.}11$, $-31^\circ\ 38'\ 23\overset{''}{.}1$ (1.3mm). Although the IR flux of the region corresponding to D2 is 50 times less than the flux of D1, it is a luminous H II region in its own right, comparable to the luminous Galactic H II region NGC 3603 or W49A or 30 Doradus in the LMC (Peck et al. 1997; De Pree et al. 2000; Smith et al. 2009), although D2 is far smaller, $\sim$ 10 pc in extent. Since it has a visible Hα region (Fig. 6), D2 may be more evolved than D1, but still young. D2 shows the 9.7μm silicate feature in emission, similar to the Orion Trapezium region or N66 in the LMC (Cesarsky et al. 2000; Whelan et al. 2013). Since D2 is located near a bright CO(3–2) cloud, D2 may be a blister H II region, although its coordinates are identical in radio continuum and CO to better than $0\overset{''}{.}1$.

3) *Region D4, H II region and GMC near D1.* Region center: $13^h\ 39^m\ 55\overset{s}{.}894$, $-31^\circ\ 38'\ 25\overset{''}{.}36$, aperture radius: $0\overset{''}{.}8$. Region D4 is associated with the CO cloud at $13^h\ 39^m\ 55\overset{s}{.}92$, $-31^\circ\ 38'\ 25\overset{''}{.}0$ (1.3mm). D4 is less distinct in MIRI/MRS continuum images due to its location near D1 and the cruciform artifact and petals of the PSF. It is located roughly $0\overset{''}{.}9$ (17 pc in projection) to the west of D1. Its proximity to the extremely luminous D1 makes D4 a fascinating object. Its relation to D1 is unclear. D4 is a brighter CO source than D1, far stronger at CO(1-0); the cloud has an H_2 mass $M_{H_2} \sim 10^6$ $M_\odot$ (including He), at least 20 times more massive than the D1 cloud. Most of the bright 870μm continuum (Fig. 6) in D4 is due to dust emission, although there is a small amount of free-free (Consiglio et al. 2017) and visible H α. Although close in projection to D1, D4 is kinematically distinct and redshifted by 15 km s^{-1} with respect to D1 (Consiglio et al. 2017). D4 has some of the strongest PAH emission in the region; it may be the effects of the radiation field of D1 on this nearby molecular cloud.

4) *Region D6, diffuse region to southwest.* Region center: $13^h\ 39^m\ 55\overset{s}{.}906$, $-31^\circ\ 38'\ 26\overset{''}{.}93$; aperture radius: $0\overset{''}{.}7$. D6 is associated with the MIR continuum source located $3\overset{''}{.}3$ ($\sim$ 60 pc) to the southwest of D1, at $13^h\ 39^m\ 55\overset{s}{.}88$, -31° $38'\ 27\overset{''}{.}4$ (1.3mm). D6 has a diffuse appearance in ALMA CO images, and extended continuum emission (Fig. 6). The H II region is clearly visible as a pointlike source in the HST/NICMOS Pa α image (Alonso-Herrero et al. 2004). D6 is associated with an arclike CO cloud and dust lane.

5) *Ellipse, covering the visible H α and Pa α plumes.* Region center: $13^h\ 39^m\ 55\overset{s}{.}952$, $-31^\circ\ 38'\ 24\overset{''}{.}42$; aperture semi-major axes: $2\overset{''}{.}6$ x $1\overset{''}{.}6$, p.a. 320. Ellipse is roughly centered on D1, chosen to encompass that portion of the bipolar "plumes" of emission evident in visible continuum, H α, and Pa α images that fall on the MIRI/MRS chip (Calzetti et al. 1997; Alonso-Herrero et al. 2004). It includes the bright arcs to the northwest. These plumes are as much of a feature of the giant supernebula as the radio core. We speculate that these plumes are emerging from holes in the D1 cloud/cluster. The arclike shapes suggest flows rather than simply escaping photons. Ellipse includes the regions D1, Clusters 5 and 11, and D4. It excludes the regions D2 and D6.

6) *Chip, covering entire footprint at 5μm.* Region center: $13^h\ 39^m\ 55\overset{s}{.}952$, $-31^\circ\ 38'\ 24\overset{''}{.}42$; aperture semi-major axes: $7''$ x $6''$, p.a. 32. This region is a polygon that follows slightly within the borders of the 5μm footprint. Because of its irregular profile, its area is actually 41.6 square arcseconds.

7) *Chip-D1, everything in the 5μm footprint except D1.* This region corresponds to the Chip region, minus the D1 region. While it may seem this could be created by subtracting D1, this region was defined so that the spectra from the region could be defringed separately from D1, although the differences in total flux turn out to be minimal.

6. CONCLUSIONS

The spatial and spectral resolution of the MIRI-MRS instrument on JWST allow us to map the dusty starburst in NGC 5253 and isolate its major mid-IR sources at parsec scales. We did a single pointing centered on the giant H II region that covers the surrounding 100 pc region. We describe the data analysis from this extremely bright mid-infrared source and present results on the continuum emission from the region surrounding the giant H II region.

- Four MIR continuum sources are detected in the central 100 pc starburst region of NGC 5253. Luminosities of these regions range from 10^7 $L_\odot$ for fainter regions NGC 5253-D2, NGC 5253-D4, and NGC 5253-D6, to 10^9 $L_\odot$ for the dominant radio-IR H II region, NGC 5253-D1, the "supernebula". The fainter H II regions are comparable in luminosity to the brightest Galactic H II regions. The regions coincide with submillimeter continuum and CO sources.

- The spectra are roughly power-law in nature; there are contributions from very small dust grains for $\lambda \lesssim 10\mu$m, classical warm H II region dust at longer wavelengths, and solid state features. Spectra of NGC 5253-D1 and

NGC 5253-D2 appear to turn over beginning at $\lambda \sim 20\mu$m, similar to Galactic compact H II regions. Solid state features, which include PAH emission and 9.7μm silicate features, are seen in all regions, but vary in intensity among them.

- The mid-IR to radio continuum flux ratio for all the H II regions, including giant H II region NGC 5253-D1, is the same as observed in the Galaxy: $S_{20\mu}/S_{2.8\mathrm{mm}} \sim 140$.
- The silicate 9.7μm absorption feature is seen in aperture NGC 5253-D1. It has an optical depth of $\tau_{9.7} \sim 0.3 \pm 0.1$ as defined by the Spoon method. Based on Galactic sources, $\tau_{9.7}$ is low for the observed extinction of $A_V \sim 15$ by factors of 2-5. The silicate 9.7μm feature is seen in emission in NGC 5253-D2, as it is in the Trapezium region of Orion (Cesarsky et al. 2000) as well as the N66 region in the LMC (Whelan et al. 2013).
- PAH emission is present in all four continuum sources. It is weakest in the giant H II region NGC 5253-D1, and strongest in NGC 5253-D4, which is associated with a molecular cloud only 15 pc in projection from the center of NGC 5253-D1. NGC 5253-D4 is the largest molecular cloud in the region and the 870μm continuum source with the largest flux. The PAH equivalent widths are a factor of 220 and 100 times weaker for the 6.2μm and 11.3μm features respectively in D1 than they are in a nearby spiral with a similar star formation rate, IC 342, but less luminous H II regions than the supernebula. Even the weaker D6 continuum source, 50 pc distant, has EW that are factors of 25 (6.2μm) and 10 (11.3μm) weaker. This demonstrates the dual factors, host metallicity and radiation field intensity/hardness that affect PAH emission.
- The primary fate of UV photons within the central 100 pc region of NGC 5253 is to emerge as MIR emission, which represents approximately half of the luminosity inferred by free-free emission within the region. This does not include an additional 25% escape fraction suggested by more extended radio emission (Rodríguez-Rico et al. 2007). Both results present evidence for porosity in the NGC 5253-D1 region; in spite of $A_v \gtrsim 15$ toward the giant H II region, 25% of even UV photons escape.
- Direct absorption of UV photons by dust within the supernebula appears to be negligible, in spite of the high extinction.

ACKNOWLEDGMENTS

We are grateful for the excellent assistance we received from the JWST help desk, the CARTA help desk, and to Eric Greisen for the continuing existence of AIPS. We thank Sergiy Silich for helpful comments on the manuscript.

Facilities: JWST(MIRI-MRS), IRSA, NED, ALMA

Software: astropy (Astropy Collaboration et al. 2013, 2018, 2022), R (R Core Team 2023), Cloudy (Ferland et al. 2017), jdaviz (Developers et al. 2025), CARTA (Comrie et al. 2025), AIPS (Greisen 1990)

REFERENCES

Aitken, D. K., Roche, P. F., Allen, M. C., & Phillips, M. M. 1982, MNRAS, 199, 31P, doi: 10.1093/mnras/199.1.31P

Alonso-Herrero, A., Takagi, T., Baker, A. J., et al. 2004, ApJ, 612, 222, doi: 10.1086/422448

Anderson, C. N. 2016, PhD thesis, New Mexico Institute of Mining and Technology

Argyriou, I., Glasse, A., Law, D. R., et al. 2023a, A&A, 675, A111, doi: 10.1051/0004-6361/202346489

Argyriou, I., Lage, C., Rieke, G. H., et al. 2023b, A&A, 680, A96, doi: 10.1051/0004-6361/202346490

Astropy Collaboration, Robitaille, T. P., Tollerud, E. J., et al. 2013, A&A, 558, A33, doi: 10.1051/0004-6361/201322068

Astropy Collaboration, Price-Whelan, A. M., Sipőcz, B. M., et al. 2018, AJ, 156, 123, doi: 10.3847/1538-3881/aabc4f

Astropy Collaboration, Price-Whelan, A. M., Lim, P. L., et al. 2022, ApJ, 935, 167, doi: 10.3847/1538-4357/ac7c74

Bastian, N., & Lardo, C. 2018, ARA&A, 56, 83, doi: 10.1146/annurev-astro-081817-051839

Beck, S. C., Lacy, J., Turner, J., et al. 2020, MNRAS, 497, 1675, doi: 10.1093/mnras/staa1819
Beck, S. C., Turner, J. L., Ho, P. T. P., Lacy, J. H., & Kelly, D. M. 1996, ApJ, 457, 610, doi: 10.1086/176757
Beck, S. C., Turner, J. L., & Zweig, E. A. 2025, ApJ
Beirão, P., Brandl, B. R., Devost, D., et al. 2006, ApJL, 643, L1, doi: 10.1086/505027
Bendo, G. J., Miura, R. E., Espada, D., et al. 2017, MNRAS, 472, 1239, doi: 10.1093/mnras/stx1837
Brandl, B. R., Bernard-Salas, J., Spoon, H. W. W., et al. 2006, ApJ, 653, 1129, doi: 10.1086/508849
Burbidge, E. M., & Burbidge, G. R. 1962, ApJ, 135, 694, doi: 10.1086/147313
Caldwell, N., & Phillips, M. M. 1989, ApJ, 338, 789, doi: 10.1086/167236
Calzetti, D., Conselice, C. J., Gallagher, John S., I., & Kinney, A. L. 1999, AJ, 118, 797, doi: 10.1086/300972
Calzetti, D., Meurer, G. R., Bohlin, R. C., et al. 1997, AJ, 114, 1834, doi: 10.1086/118609
Calzetti, D., Johnson, K. E., Adamo, A., et al. 2015, ApJ, 811, 75, doi: 10.1088/0004-637X/811/2/75
Cesarsky, D., Jones, A. P., Lequeux, J., & Verstraete, L. 2000, A&A, 358, 708, doi: 10.48550/arXiv.astro-ph/0002282
Chiar, J. E., & Tielens, A. G. G. M. 2006, ApJ, 637, 774, doi: 10.1086/498406
Chown, R., Sidhu, A., Peeters, E., et al. 2024, A&A, 685, A75, doi: 10.1051/0004-6361/202346662
Cohen, D. P., Turner, J. L., Consiglio, S. M., Martin, E. C., & Beck, S. C. 2018, ApJ, 860, 47, doi: 10.3847/1538-4357/aac170
Comrie, A., Wang, K.-S., Hwang, Y.-H., et al. 2025, CARTA: The Cube Analysis and Rendering Tool for Astronomy, 5.0, Zenodo, doi: 10.5281/zenodo.17050846
Consiglio, S. M., Turner, J. L., Beck, S., et al. 2017, ApJ, 850, 54, doi: 10.3847/1538-4357/aa93dc
Cresci, G., Vanzi, L., & Sauvage, M. 2005, A&A, 433, 447, doi: 10.1051/0004-6361:20041028
Crowther, P. A., Beck, S. C., Willis, A. J., et al. 1999, MNRAS, 304, 654, doi: 10.1046/j.1365-8711.1999.02380.x
de Grijs, R., Anders, P., Zackrisson, E., & Östlin, G. 2013, MNRAS, 431, 2917, doi: 10.1093/mnras/stt392
De Pree, C. G., Wilner, D. J., Goss, W. M., Welch, W. J., & McGrath, E. 2000, ApJ, 540, 308, doi: 10.1086/309315
Developers, J., Averbukh, J., Bradley, L., et al. 2025, Jdaviz, v4.4.1, Zenodo, doi: 10.5281/zenodo.17211099
Dicken, D., Marín, M. G., Shivaei, I., et al. 2024, A&A, 689, A5, doi: 10.1051/0004-6361/202449451
Draine, B. T., & Li, A. 2007, ApJ, 657, 810, doi: 10.1086/511055
Draine, B. T., Li, A., Hensley, B. S., et al. 2021, ApJ, 917, 3, doi: 10.3847/1538-4357/abff51
Ferland, G. J., Chatzikos, M., Guzmán, F., et al. 2017, RMxAA, 53, 385, doi: 10.48550/arXiv.1705.10877
Gasman, D., Argyriou, I., Sloan, G. C., et al. 2023, A&A, 673, A102, doi: 10.1051/0004-6361/202245633
Gáspár, A., Rieke, G. H., Guillard, P., et al. 2021, PASP, 133, 014504, doi: 10.1088/1538-3873/abcd04
Genzel, R., Becklin, E. E., Wynn-Williams, C. G., et al. 1982, ApJ, 255, 527, doi: 10.1086/159853
Gibb, E. L., Whittet, D. C. B., Boogert, A. C. A., & Tielens, A. G. G. M. 2004, ApJS, 151, 35, doi: 10.1086/381182
Gordon, K. D., Clayton, G. C., Decleir, M., et al. 2023, ApJ, 950, 86, doi: 10.3847/1538-4357/accb59
Gordon, K. D., Chen, C. H., Anderson, R. E., et al. 2015, PASP, 127, 696, doi: 10.1086/682260
Gordon, K. D., Misselt, K. A., Bouwman, J., et al. 2021, ApJ, 916, 33, doi: 10.3847/1538-4357/ac00b7
Gorjian, V. 1996, AJ, 112, 1886, doi: 10.1086/118150
Gorjian, V., Turner, J. L., & Beck, S. C. 2001, ApJL, 554, L29, doi: 10.1086/320923
Graham, J. A. 1981, PASP, 93, 552, doi: 10.1086/130884
Greisen, E. W. 1990, in Acquisition, Processing and Archiving of Astronomical Images, 125–142
Harris, J., Calzetti, D., Gallagher, John S., I., Smith, D. A., & Conselice, C. J. 2004, ApJ, 603, 503, doi: 10.1086/381669
Hodge, P. W. 1966, ApJ, 146, 593, doi: 10.1086/148927
Hunt, L., Bianchi, S., & Maiolino, R. 2005, A&A, 434, 849, doi: 10.1051/0004-6361:20042157
Hunt, L. K., Thuan, T. X., Izotov, Y. I., & Sauvage, M. 2010, ApJ, 712, 164, doi: 10.1088/0004-637X/712/1/164
Hunt, L. K., Weiß, A., Henkel, C., et al. 2017, A&A, 606, A99, doi: 10.1051/0004-6361/201731000
Inoue, A. K. 2001, AJ, 122, 1788, doi: 10.1086/323095
Inoue, A. K., Hirashita, H., & Kamaya, H. 2001, ApJ, 555, 613, doi: 10.1086/321499
Karachentsev, I. D., Makarov, D. I., & Kaisina, E. I. 2013, AJ, 145, 101, doi: 10.1088/0004-6256/145/4/101
Karachentsev, I. D., Tully, R. B., Dolphin, A., et al. 2007, AJ, 133, 504, doi: 10.1086/510125
Kawara, K., Nishida, M., & Phillips, M. M. 1989, ApJ, 337, 230, doi: 10.1086/167099
Kobulnicky, H. A., & Skillman, E. D. 1995, ApJL, 454, L121, doi: 10.1086/309791
—. 2008, AJ, 135, 527, doi: 10.1088/0004-6256/135/2/527
Kobulnicky, H. A., Skillman, E. D., Roy, J.-R., Walsh, J. R., & Rosa, M. R. 1997, ApJ, 477, 679, doi: 10.1086/303742

Lai, T. S. Y., Smith, J. D. T., Baba, S., Spoon, H. W. W., & Imanishi, M. 2020, ApJ, 905, 55, doi: 10.3847/1538-4357/abc002

Lai, T. S. Y., Duval, S., Smith, J. D. T., et al. 2025, arXiv e-prints, arXiv:2509.04662, doi: 10.48550/arXiv.2509.04662

Law, D. R., E. Morrison, J., Argyriou, I., et al. 2023, AJ, 166, 45, doi: 10.3847/1538-3881/acdddc

Lebouteiller, V., Brandl, B., Bernard-Salas, J., Devost, D., & Houck, J. R. 2007, ApJ, 665, 390, doi: 10.1086/519014

Leitherer, C., Schaerer, D., Goldader, J. D., et al. 1999, ApJS, 123, 3, doi: 10.1086/313233

López-Sánchez, Á. R., Koribalski, B. S., van Eymeren, J., et al. 2012, MNRAS, 419, 1051, doi: 10.1111/j.1365-2966.2011.19762.x

Martín-Hernández, N. L., Schaerer, D., & Sauvage, M. 2005, A&A, 429, 449, doi: 10.1051/0004-6361:20041603

Mathis, J. S., Mezger, P. G., & Panagia, N. 1983, A&A, 128, 212

Meier, D. S., Turner, J. L., & Beck, S. C. 2002, AJ, 124, 877, doi: 10.1086/341752

Miura, R. E., Espada, D., Hirota, A., et al. 2018, ApJ, 864, 120, doi: 10.3847/1538-4357/aad69f

Mohan, N. R., Anantharamaiah, K. R., & Goss, W. M. 2001, ApJ, 557, 659, doi: 10.1086/322265

Monreal-Ibero, A., Vílchez, J. M., Walsh, J. R., & Muñoz-Tuñón, C. 2010, A&A, 517, A27, doi: 10.1051/0004-6361/201014154

Moorwood, A. F. M., & Glass, I. S. 1982, A&A, 115, 84

Peck, A. B., Goss, W. M., Dickel, H. R., et al. 1997, ApJ, 486, 329, doi: 10.1086/304508

Peeters, E., Allamandola, L. J., Hudgins, D. M., Hony, S., & Tielens, A. G. G. M. 2004, in Astronomical Society of the Pacific Conference Series, Vol. 309, Astrophysics of Dust, ed. A. N. Witt, G. C. Clayton, & B. T. Draine, 141, doi: 10.48550/arXiv.astro-ph/0312184

Peeters, E., Martín-Hernández, N. L., Damour, F., et al. 2002, A&A, 381, 571, doi: 10.1051/0004-6361:20011516

Pickering, E. 1895, Bull. Harvard College Obs.

R Core Team. 2023, R: A Language and Environment for Statistical Computing, R Foundation for Statistical Computing, Vienna, Austria. https://www.R-project.org/

Rémy-Ruyer, A., Madden, S. C., Galliano, F., et al. 2013, A&A, 557, A95, doi: 10.1051/0004-6361/201321602

—. 2015, A&A, 582, A121, doi: 10.1051/0004-6361/201526067

Rodríguez-Rico, C. A., Goss, W. M., Turner, J. L., & Gómez, Y. 2007, ApJ, 670, 295, doi: 10.1086/520709

Schaerer, D., Contini, T., Kunth, D., & Meynet, G. 1997, ApJL, 481, L75, doi: 10.1086/310659

Silich, S., Tenorio-Tagle, G., Martínez-González, S., & Turner, J. 2020, MNRAS, 494, 97, doi: 10.1093/mnras/staa705

Silich, S., Tenorio-Tagle, G., & Rodríguez-González, A. 2004, ApJ, 610, 226, doi: 10.1086/421702

Smith, L. J., Bajaj, V., Ryon, J., & Sabbi, E. 2020, ApJ, 896, 84, doi: 10.3847/1538-4357/ab8f94

Smith, L. J., Crowther, P. A., Calzetti, D., & Sidoli, F. 2016, ApJ, 823, 38, doi: 10.3847/0004-637X/823/1/38

Smith, N., Whitney, B. A., Conti, P. S., de Pree, C. G., & Jackson, J. M. 2009, MNRAS, 399, 952, doi: 10.1111/j.1365-2966.2009.15343.x

Spoon, H. W. W., Marshall, J. A., Houck, J. R., et al. 2007, ApJL, 654, L49, doi: 10.1086/511268

Stock, D. J., Peeters, E., Choi, W. D. Y., & Shannon, M. J. 2014, ApJ, 791, 99, doi: 10.1088/0004-637X/791/2/99

Tenorio-Tagle, G., Silich, S., Rodríguez-González, A., & Muñoz-Tuñón, C. 2005, ApJL, 628, L13, doi: 10.1086/432665

Turner, J. L., & Beck, S. C. 2004, ApJL, 602, L85, doi: 10.1086/382699

Turner, J. L., Beck, S. C., Benford, D. J., et al. 2015, Nature, 519, 331, doi: 10.1038/nature14218

Turner, J. L., Beck, S. C., Crosthwaite, L. P., et al. 2003, Nature, 423, 621, doi: 10.1038/nature01689

Turner, J. L., Beck, S. C., & Ho, P. T. P. 2000, ApJL, 532, L109, doi: 10.1086/312586

Turner, J. L., Beck, S. C., & Hurt, R. L. 1997, ApJL, 474, L11, doi: 10.1086/310412

Turner, J. L., Consiglio, S. M., Beck, S. C., et al. 2017, ApJ, 846, 73, doi: 10.3847/1538-4357/aa8669

Turner, J. L., Ho, P. T. P., & Beck, S. C. 1998, AJ, 116, 1212, doi: 10.1086/300485

Vanzi, L., & Sauvage, M. 2004, A&A, 415, 509, doi: 10.1051/0004-6361:20034635

Verma, A., Lutz, D., Sturm, E., et al. 2003, A&A, 403, 829, doi: 10.1051/0004-6361:20030408

Walsh, J. R., & Roy, J.-R. 1989, MNRAS, 239, 297, doi: 10.1093/mnras/239.2.297

Wells, M., Pel, J. W., Glasse, A., et al. 2015, PASP, 127, 646, doi: 10.1086/682281

Whelan, D. G., Lebouteiller, V., Galliano, F., et al. 2013, ApJ, 771, 16, doi: 10.1088/0004-637X/771/1/16

Whittet, D. C. B. 1992, Dust in the galactic environment

Wood, D. O. S., & Churchwell, E. 1989, ApJS, 69, 831, doi: 10.1086/191329

Wu, Y., Charmandaris, V., Hao, L., et al. 2006, ApJ, 639, 157,
doi: 10.1086/49922610.48550/arXiv.astro-ph/0510856

Zastrow, J., Oey, M. S., Veilleux, S., McDonald, M., & Martin, C. L. 2011, ApJL, 741, L17,
doi: 10.1088/2041-8205/741/1/L17